European Journal of Medicinal Chemistry 276 (2024) 116642

Contents lists available at ScienceDirect

European Journal of Medicinal Chemistry

journal homepage: www.elsevier.com/locate/ejmech

Research paper

Structure-based mapping of the histone-binding pocket of KDM4D using functionalized tetrazole and pyridine core compounds

Piotr H. Małecki [a,b,c,*], Georg M. Fassauer [d], Nicole Rüger [d], Lukas Schulig [d], Andreas Link [d], Oxana Krylova [e], Udo Heinemann [a], Manfred S. Weiss [b]

[a] Macromolecular Structure and Interaction, Max-Delbrück-Center for Molecular Medicine, Robert-Rössle-Str. 10, 13125, Berlin, Germany
[b] Macromolecular Crystallography, Helmholtz-Zentrum Berlin für Materialien und Energie, Albert-Einstein-Str. 15, 12489, Berlin, Germany
[c] Department of Structural Biology of Prokaryotic Organisms, Institute of Bioorganic Chemistry, Polish Academy of Sciences, Z. Noskowskiego-Str. 12/14, 61-704, Poznań, Poland
[d] Department of Pharmaceutical and Medicinal Chemistry, Institute of Pharmacy, Universität Greifswald, Friedrich-Ludwig-Jahn-Straße 17, 17489, Greifswald, Germany
[e] Department of Molecular Biophysics, Leibniz-Forschungsinstitut für Molekulare Pharmakologie, Robert-Rössle-Str. 10, 13125, Berlin, Germany

ARTICLE INFO

Keywords:
Structure-based screening
Protein surface mapping
Flexible ligands
Cancer
Drug discovery
Inhibitors
Lysine demethylases
KDM4

ABSTRACT

KDM4 histone demethylases became an exciting target for inhibitor development as the evidence linking them directly to tumorigenesis mounts. In this study, we set out to better understand the binding cavity using an X-ray crystallographic approach to provide a detailed landscape of possible interactions within the under-investigated region of KDM4. Our design strategy was based on utilizing known KDM binding motifs, such as nicotinic acid and tetrazolylhydrazides, as core motifs that we decided to enrich with flexible tails to map the distal histone binding site. The resulting X-ray structures of the novel compounds bound to KDM4D, a representative of the KDM4 family, revealed the interaction pattern with distal residues in the histone-binding site. The most prominent protein rearrangement detected upon ligand binding is the loop movement that blocks the accessibility to the histone binding site. Apart from providing new sites that potential inhibitors can target, the novel compounds may prove helpful in exploring the capacity of ligands to bind in sites distal to the cofactor-binding site of other KDMs or 2-oxoglutarate (2OG)-dependent oxygenases. The case study proves that combining a strong small binding motif with flexible tails to probe the binding pocket will facilitate lead discovery in classical drug-discovery campaigns, given the ease of accessing X-ray quality crystals.

1. Introduction

In recent years, research focused on epigenetic mechanisms has attracted considerable attention in the area of gene regulation. Epigenetic processes mediate phenotypic changes by altering the genome without changing the DNA sequence. Epigenetic control is exerted by chemical changes in DNA itself, reversible histone tail modifications, including acetylation, methylation, phosphorylation, or ubiquitination, ultimately shaping the chromatin state and affecting the accessibility of genes to transcription factors. As a result, epigenetic mechanisms influence cellular homeostasis, health, inheritance, biological adaptivity, and plasticity [1,2].

Research into the multiple associations of epigenetics with the causation and progression of various diseases has progressed significantly and has tapped into applications in the clinic. Still, epigenetic marks, as potentially heritable, environmentally influenced elements of gene regulation, are not entirely understood [3]. In this respect, small organic molecules play a significant role in targeting enzymes involved in writing, reading, or erasing chemical modifications of chromatin. Many of these are currently investigated in pharmaceutical pipelines. This is particularly true for histone deacetylase inhibitors (HDACIs) [4]. Research into the post-translational methylation and demethylation of

Abbreviations: KDM, lysine demethylase; 2OG, 2-oxoglutarate; HDACI, histone deacetylase inhibitors; KMT, lysine methyl transferase; FAD, flavin adenine dinucleotide; LSD, lysine-specific demethylases; JmjC, Jumanji C domain; HQ, hydroxyquinoline; 2,4-PDCA, pyridine-2,4-dicarboxylic acid; μW, microwave (not to be confused with microwatt).

* Corresponding author. Department of Structural Biology of Prokaryotic Organisms, Institute of Bioorganic Chemistry Polish Academy of Sciences, Z. Noskowskiego-Str. 12/14, 61-704 Poznań, Poland
E-mail address: pimalecki@ibch.poznan.pl (P.H. Małecki).

https://doi.org/10.1016/j.ejmech.2024.116642
Received 7 March 2024; Received in revised form 28 June 2024; Accepted 29 June 2024
Available online 2 July 2024

Lys and Arg residues of histones' N- and C-terminal tails is less advanced, even though this modification is strongly linked to tumorigenesis. The histone methylation state is regulated by lysine methyl transferases (KMT) and lysine demethylases (KDM). The cellular activity of these two enzymes needs to be tightly regulated to maintain a reversible and balanced state [5]. Dysregulation of the methylation pattern of various lysine residues, e.g., H3K9me2 [6], H3K9me3 [7], H3K27me2 [8], H3K36me2/me3 [9] is associated with several types of cancers, ranging from prostate to ovarian and breast cancers.

Human KDMs are classified into two classes based on their catalytic mechanism. The first class comprises the FAD-dependent lysine-specific demethylases (LSD), and the second, larger group, the Jumanji C (JmjC) domain-containing KDMs, which are 2-oxoglutarate (2OG, also called α-ketoglutarate, or α-KG) and Fe^{2+} dependent. In the latter class of KDMs, 2OG chelates the catalytic Fe^{2+} cation and is later decarboxylated to succinate while the methyl group of the substrate mono-, di- or trimethylated lysine residue is first oxidized to a hemiaminal and then hydrolyzed non-catalytically to formaldehyde and water [10].

The KDM4 demethylases constitute a subfamily of the 2OG-dependent KDMs, which consists of five functional enzymes, KDM4A-E. A sixth gene (*KDM4F)* has been identified but is considered a pseudogene [11,12]. While the catalytically active JmjC domain is present in all members of the KDM4 family, KDM4D and KDM4E are distinguished by the lack of the plant homeodomains (PHD) and Tudor domains (TD) present in the other KDM4s [13]. *KDM4* genes are expressed in tissues like the spleen, ovary, and testis under physiological conditions [14,15]. Elevated expression of *KDM4* is connected with various diseases, including several malignancies, e.g., breast [16] or ovarian cancer [17]. KDM4 proteins are directly involved in tumorigenesis, and as such, they are promising targets for anticancer therapies. According to the catalytic mechanism of the JmjC domain-containing enzymes, many of the enzyme inhibitors that have been characterized so far are 2OG cofactor mimics. However, other known mechanisms for KDM inhibition, such as the displacement of an active-site metal ion [18] or competitive binding to the histone-binding site [19] exist. The current state of the development of KDM inhibitors was summarized in recent reviews [20–22].

Numerous crystal structures of subfamily members revealed that KDM4 proteins are structurally conserved concerning their catalytic domain and the associated 2OG binding site. In all KDM4s, the binding site for histone is located close to the cavity entrance, while the methylated lysine residue binds deeper next to the 2OG binding site. As mentioned above, most of the reported KDM ligands are 2OG-cofactor competitors that chelate the active-site metal ion on one side and block the key residues typically engaged in cofactor binding on the other side. Among those inhibitors, there are close analogs of 2OG, *N*-oxalylglycine (NOG) [23], 2OG hydroxamate derivatives [24], pyridine carboxylate and dicarboxylate derivatives, hydroxyquinoline (HQ) based inhibitors [25] and others. Many attempts have been made to optimize the ligands and improve their ability to permeate through membranes [26]. One common strategy is to replace the hydrophilic carboxylic acid moieties with more (by a factor of ten) lipophilic moieties like tetrazoles to improve the physicochemical properties of the compounds [27,28].

To improve the selectivity of the inhibitors, the more distal areas of the histone binding site, which differ among KDM4 members, may be exploited. This could be achieved by employing a set of molecules that could map the probable interactions within the histone binding site to delineate a set of possible ligand-protein interactions essential for further ligand optimization. Usually, crystallographic fragment screening employs a small molecule library to probe the binding pockets of the targeted protein [29,30]. The major drawback is the low affinity of the fragments to the target, which results in fewer identified interactions in a protein's site of interest. Herein, we propose using an alternative, directed method by creating a novel set of compounds based on a known compound core targeting the 2OG binding site containing additional alternative diverse, flexible extensions. The strategy overcomes the binding barriers by facilitating probing the vicinity of the protein-bound core motif. The compounds were synthesized and structurally characterized in complex with KDM4D. Some of the ligands were further characterized by isothermal titration calorimetry. These molecular probes could eventually be utilized to develop more potent and selective inhibitors to accelerate other 2OG-dependent oxygenase drug development.

2. Materials and methods

2.1. Ligand synthesis

All solvents and reagents were obtained from commercial suppliers (Sigma Aldrich, VWR, or ABCR) and used without prior purification. Anhydrous solvents were purchased from Acros Organics. Microwave-assisted syntheses were performed using an Anton Paar Monowave 300 reactor operated in closed vessel mode using G30-vials with 20 mL total capacity; temperature control was performed via integrated IR sensor, stirring speed was 600 rpm. Thin layer chromatography (TLC) was executed on pre-coated silica gel 60 F_{254} aluminum foil sheets purchased from Merck. Visualization of compounds invisible to the naked eye was accomplished by UV light (254 nm and 366 nm). Preparative column chromatography at ambient pressure was done on silica gel from Macherey-Nagel (particle size 50–100 μm, 140–270 mesh ASTM). Purification of products by flash chromatography was performed on silica gel (20–45 μm from Carl Roth), applying pressured air up to 0.8 bar. NMR spectra were recorded on a Bruker Avance III instrument (^{1}H NMR: 400 MHz, ^{13}C NMR: 100.6 MHz). Chemical shifts were referenced to tetramethylsilane (TMS) as internal standard in deuterated solvents and reported in parts per million (ppm). Coupling constants (*J*) are reported in Hz using the abbreviations: br = broad, s = singlet, d = doublet, t = triplet, q = quartet, m = multiplet, and combinations thereof. Mid-infrared spectra were recorded on an ALPHA FT-IR instrument from Bruker Optics or on a Nicolet IR200 FT-IR from Thermo Electron Corporation, both equipped with a diamond ATR accessory unit, and are indicated in terms of absorption frequency [cm^{-1}]. Melting points were measured in open capillary tubes using a Melting Point M − 565 apparatus from Büchi and were uncorrected. High-accuracy mass spectra were recorded on a Shimadzu LCMS-IT-TOF using ESI ionization. The purity of the final compounds was determined by HPLC with DAD (applying the 100 % method at 220 nm and 254 nm). Preparative and analytical HPLC were performed using Shimadzu devices CBM-20 A, LC-20 A P, SIL-20 A, FRC-10 A with SPD 20 A UV/Vis detector and an ELSD-LT II. In analytical mode, a LiChroCART (250 × 4 mm) and in preparative mode, a Hibar RT (250 × 25 mm) column were used, both containing LiChrospher 100 RP-18 endcapped (5 μm). All compounds are >95 % pure by HPLC analysis. All synthesized ligands were deposited at the EU-OPENSCREEN screening site in Berlin to provide a compound set of metal chelating agents, useful as a toolkit for further investigations on miscellaneous protein targets.

2.1.1. Synthesis of compound 1 (2-[(3-hydroxypropyl)amino]isonicotinic acid)

A mixture of 2-chloro isonicotinic acid (**11**, 1.0 g, 7.2 mmol) and 3-aminopropan-1-ol (10 mL, 130 mmol) was stirred in a round-bottom flask for 22 h at 120 °C. Subsequently, the reaction mixture was diluted with demineralized water (50 mL) and concentrated hydrochloric acid (25 mL). An acidic pH of 1–2 resulted, and heating to reflux was maintained for 16 h. The total volume was reduced to approximately one quarter under reduced pressure, and the residual volume was cooled to 5 °C to initiate crystallization. After 12 h, the solid was collected, washed with tetrahydrofuran, dissolved in water, and purified by preparative HPLC (C18 column, 250 × 25 mm, eluents: A: H_2O and B: MeOH, isocratic, 30 % B) and freeze-dried to afford a colorless amorphous powder (366 mg, 26 % yield). ^{1}H NMR (DMSO-d_6): δ ppm = 1.73 (m, 2H, J = 6.4 Hz), 3.39 (s, 2H), 3.50 (t, 2H, J = 6.4 Hz), 6.96 (d, 1H, J

= 5.6 Hz), 7.28 (s, 1H), 8.02 (d, 1H, J = 5.6 Hz), 8.14 (s, 1H); ^{13}C NMR (DMSO-d_6): δ ppm = 31.5, 38.6, 58.1, 109.8, 111.7, 140.8, 142.4, 156.3, 165.5; FTIR ($\tilde{\nu}$): 3240 (m, $\nu_{O\text{-}H}$), 3182 (m, $\nu_{N\text{-}H}$), 1713 (s, $\nu_{C=O}$) cm^{-1}. HRMS (ESI): calcd for $C_9H_{13}N_2O_3$ [M + H]$^+$ *m/z*, 197.0921; found *m/z*, 197.0914; mp range 194–196 °C.

2.1.2. Synthesis of compound 2 (2-{[2-(methanesulfonamido)ethyl] amino}isonicotinic acid)

2-[(2-Aminoethyl)amino]isonicotinic acid hydrochloride (**12**, 400 mg, 1.8 mmol, was suspended in acetonitrile (10 mL). Dilute NaOH solution was added until a clear solution was obtained. During cooling with ice, methanesulfonyl chloride (420 μL, 5.4 mmol) was added dropwise. Subsequently, the mixture was stirred at room temperature for 20 h. Volatiles were removed under reduced pressure, and the residue was purified by column chromatography (EtOAc/methanol/ammonia solution 60:40:1 v/v/v). The obtained product-containing fractions were freed from the mobile phase and finally purified by preparative HPLC (C18 column, 250 × 25 mm, A: water with 0.1 % acetic acid and B: methanol, isocratic, 10 % B) and freeze-dried to afford a colorless amorphous powder (186 mg, 29 % yield). A sample for melting range determination was crystallized from EtOH (EtOH/water, 95:5, v/v). ^{1}H NMR (DMSO-d_6): δ ppm = 2.89 (s, 3H), 3.10 (t, 2H, J = 6.4 Hz), 3.39 (t, 2H, J = 6.4 Hz), 6.88 (d, 1H, J = 5.6 Hz), 6.97 (m, 2H), 7.09 (d, 1H, J = 6.0 Hz), 8.10 (s, 1H), 13.25 (s, 1H); ^{13}C NMR (DMSO-d_6): δ ppm = 39.5, 40.9, 41.8, 108.5, 110.3, 138.8, 148.4, 159.1, 166.7; FTIR ($\tilde{\nu}$): 3156 (m, $\nu_{N\text{-}H}$), 1677 (s, $\nu_{C=O}$) cm^{-1}. HRMS (ESI): calcd for $C_9H_{14}N_3O_4S$ [M + H$^+$] *m/z*, 260.0700; found *m/z*, 260.0694; mp range 273–275 °C (decomposition).

2.1.3. Synthesis of compound 3 (N-(3-morpholinopropyl)-4-(1H-tetrazol-5-yl)picolinamide hydrochloride)

4-(1*H*-Tetrazol-5-yl)picolinic acid ethyl ester (**13**, 915 mg, 4.1 mmol) and 3-morpholinopropylamine (3.0 mL, 20.5 mmol) in EtOH (15 mL) were sealed in an Anton Paar G30 tube and heated by means of microwave irradiation to 165 °C for 45 min while stirring in an Anton Paar Monowave 300. After cooling to room temperature, the tube was opened, and the contents diluted with EtOH to a total volume of 80 mL and acidified by the addition of hydrochloric acid (36 %). Upon standing at −21 °C, precipitation occurred during 1 h. Solids were collected by filtration and recrystallized from EtOH twice. The obtained product was washed vigorously with toluene, tetrahydrofuran, and acetone, in this order. After drying, a colorless amorphous product was obtained and dried (233 mg, 18 % yield). ^{1}H NMR (DMSO-d_6): δ ppm = 2.30 (m, 2H, J = 8.0 Hz), 3.06 (s, 2H), 3.14 (m, 2H, J = 8.0 Hz), 3.43 (m, 4H), 3.85 (2 × s, 2 × 2H), 8.27 (d, 1H, J = 4.8 Hz), 8.67 (s, 1H), 8.88 (d, 1H, J = 5.2 Hz), 9.16 (t, 1H), 10.98 (s, 1H); ^{13}C NMR (DMSO-d_6): δ = 23.4, 36.3, 50.9, 53.9, 63.2, 118.9, 123.3, 133.9, 149.8, 151.1, 155.1, 163.5; FTIR ($\tilde{\nu}$): 3344 (s, $\nu_{N\text{-}H}$), 1644 (s, $\nu_{C=O}$), 1613 (s, $\nu_{C=N}$) cm^{-1}. HRMS (ESI): calcd for $C_{14}H_{20}N_7O_2$ [M + H]$^+$ *m/z*, 318.1673; found *m/z*, 318.1664; mp range 129–130 °C.

2.1.4. Synthesis of compound 4 (N-hydroxy-4-(1H-tetrazol-5-yl) picolinamide)

4-(1*H*-Tetrazol-5-yl)picolinic acid (**15**,200 mg, 1.0 mmol) was dissolved in DMF (10 mL) and stirred in an ice bath. After addition of oxalyl chloride (120 μL, 1.4 mmol), stirring was continued for 30 min. Subsequently, excess oxalyl chloride was removed *in vacuo,* and DIPEA (525 μL, 3 mmol) was added, followed by addition of hydroxylamine hydrochloride (100 mg, 1.4 mmol). The reaction proceeded at room temperature for 18 h. The resulting solution was diluted with EtOH (10 mL) and water (10 mL). The mixture was acidified with hydrochloric acid (36 %), resulting in precipitation of 4-(1*H*-tetrazol-5-yl)picolinic acid (**15**). The precipitate was collected and dissolved in a solution of ammonia in MeOH, adsorbed on diatomaceous earth, and purified by column chromatography (eluent EtOAc/MeOH/acetic acid, 50:50:1, v/v/v). Product containing fractions were combined and evaporated. The obtained residue was crystallized from water and dried to afford colorless crystals (45 mg, 21 % yield). ^{1}H NMR (DMSO-d_6): δ ppm = 8.18 (d, 1H, J = 5.2 Hz), 8.60 (s, 1H), 8.85 (d, 1H, J = 5.2 Hz), 9.23 (s, 1H), 11.64 (s, 1H); ^{13}C NMR (DMSO-d_6): δ ppm = 118.8, 123.0, 133.8, 149.9, 151.3, 154.8, 160.6; FTIR ($\tilde{\nu}$): 3335 (m, $\nu_{N\text{-}H}$), 1643 (s, $\nu_{C=O}$), 1610 (s, $\nu_{C=N}$) cm^{-1}. HRMS (ESI): calcd for $C_7H_7N_6O_2$ [M + H]$^+$ *m/z*, 207.0625; found *m/z*, 207.0617; mp range 241–242 °C (decomposition).

2.1.5. Synthesis of compound 5 N-[2-hydrazino-2-oxo-1-(1H-tetrazol-5-yl)ethyl]-4-bromo benzamide)

4-Bromo-*N*-{2-[2(*E/Z*)-(butan-2-ylidene)hydrazinyl]-2-oxo-1-(1*H*-tetrazol-5-yl)ethyl}benzamid (**18**, 230 mg, 5.70 mmol) was dissolved in boiling EtOH (50 mL) and treated with an aqueous ammonia solution (25 % NH_3 in water, 15 mL) under reflux. The mixture was kept under reflux for 5 h and subsequently concentrated *in vacuo*. Residual ammonia, water, and butanone were removed by multiple azeotropic drying with EtOH. The resulting solid was filtered over a G4 glass filter funnel, washed with EtOH, and dried for 18 h at 8 mbar and 60 °C to yield a colorless solid (190 mg, 97 %). Crystallization from 2-propanol yielded a colorless solid (70 mg, 38 %). ^{1}H NMR DMSO-d_6): δ ppm = 5.80 (d, 1H, C (3)H, ^3J = 8.0 Hz), 7.67–7.69 (m, 2H), 7.84–7.86 (m, 2H), 8.65 (d, 1H, NH, ^3J = 8.0 Hz), 9.34 (s, 1H, NH). ^{13}C NMR (DMSO-d_6): δ ppm = 62.0, 125.1, 129.7, 131.3, 133.1, 157.7, 164.8, 168.4. FTIR ($\tilde{\nu}$) = 1639 (m, $\nu_{C=O}$) cm^{-1}. HRMS (ESI): calcd for $C_{10}H_9N_7O_2Br$ [M − H]$^-$ *m/z*, 338.0007; found *m/z*, 338.0004; mp range 168–170 °C.

2.1.6. Synthesis of compound 6 (N-[(1R,S)-2-hydrazinyl-2-oxo-1-(1H-tetrazol-5-yl)ethyl]-5-phenylvaleramide)

N-{2-Oxo-2-[2-(propan-2-yliden)hydrazinyl]-1-(1*H*-tetrazol-5-yl) ethyl}-5-phenylvaleramide (**15**, 300 mg, 0.84 mmol) was dissolved in boiling EtOH (50 mL) and treated with an aqueous ammonia solution (25 % NH_3 in water, 15 mL) under reflux. The mixture was kept under reflux for 5 h and subsequently concentrated *in vacuo*. Residual ammonia, water, and acetone were removed by multiple azeotropic drying with EtOH. The resulting solid was filtered over a G4 glass filter funnel, washed with EtOH, and dried for 18 h at 8 mbar and 60 °C to yield a colorless solid (20 mg, 6 %). ^{1}H NMR DMSO-d_6): δ ppm = 1.52 (s, 4H), CH_2), 2.24–2.27 (m, 2H, C (9)H_2), 2.54–2.58 (m, 2H, CH_2), 5.81 (d, 1H, CH, ^3J = 8.0 Hz), 7.14–7.18 (m, 3H, 3 × CH), 7.25–7.28 (m, 2H, 2 × CH), 8.70 (d, 1H, NH, ^3J = 7.6 Hz), 9.63 (s, 1H, NH). ^{13}C NMR (DMSO-d_6): δ ppm = 24.5, 30.5, 34.5, 34.8, 46.9, 125.6, 128.2, 128.3, 142.1, 165.5, 172.5. FTIR ($\tilde{\nu}$) = 1520 (w, $\nu_{C=C}$), 1644 (m, $\delta_{N\text{-}H}$) cm^{-1}. HRMS (ESI): calcd for $C_{14}H_{18}N_7O_2$ [M − H]$^-$ *m/z*, 316.1527; found *m/z*, 316.1516; mp range 170–173 °C.

2.1.7. Synthesis of compounds 7, 8, 9 and 10

Compounds **7**–**10** were prepared exactly as already described in the cited literature [28,31].

2.1.8. Synthesis of compound 11 (2-chloroisonicotinic acid)

Commercially available 2-chloroisonicotinonitrile (2.8 g, 20 mmol) was dissolved in ethanol (20 mL). Aqueous NaOH (2.4 g, 60 mmol, dissolved in 10 mL water) was added to the solution. The reaction mixture was refluxed for 3 h. Completion of the reaction was observed when the odor of ammonia ceased. All volatiles were removed under reduced pressure, yielding a white solid, which was washed with ethyl acetate. The residue was dissolved in water and precipitated with HCl. The solid was filtered off and recrystallized from water to yield a colorless solid (2.0 g, 64 %). FTIR ($\tilde{\nu}$): 1707 (s), 1367 (s) cm^{-1}. ^{1}H NMR (DMSO-d_6): δ ppm = 7.83 (d, 2H, J = 4.8 Hz), 8.61 (s, 1H, J = 4.8 Hz), 14.01 (s, 1H); ^{13}C NMR (DMSO-d_6): δ = 122.2, 123.5, 141.8, 151.1, 164.8; mp range: 235–236 °C (234–235 °C) [32].

2.1.9. Synthesis of compound 12 (2-[(2-aminoethyl)amino]isonicotinic acid hydrochloride)

2-Chloroisonicotinic acid (**11**, 1.4 g, 8.9 mmol) was combined with

ethane-1,2-diamine (5.9 mL, 89 mmol) in a microwave reactor tube and heated at 180 °C for 60 min in the microwave reactor. Excess of diamine was subsequently removed under reduced pressure at 70 °C. The resulting residue was treated with HCl (36 %) and suspended in methanol. The slurry was filtered and the solid was discarded. The resulting filtrate was evaporated under reduced pressure. Addition of 15 mL HCl (25 %) and refluxing for 3 h cleaved the potentially generated amide. The volume of the cleavage mixture was reduced to one-half. While storing at 8 °C for a couple of hours, the desired product precipitated out of the acidic solution. The solid was filtered off and finally washed with THF/diethyl ether (1:1) yielding a colorless solid (1.39 g, 72 %); ^{1}H NMR (D_2O): δ ppm = 3.28 (t, 2H, J = 6.4 Hz), 3.75 (t, 2H, J = 6.0 Hz), 7.27 (d, 1H, J = 6.4 Hz), 7.53 (s, 1H), 7.90 (d, 1H, J = 6.4 Hz); ^{13}C NMR (D_2O): δ ppm = 37.6, 39.5, 112.1, 136.4, 145.8, 153.3, 166.6; FTIR ($\tilde{\nu}$): 3348 (m), 1727 (s) cm^{-1}.; HRMS (ESI): calcd for $C_8H_{10}N_3O_2$ $[M - H]^-$ m/z, 180.0779; found m/z, 180.0779; mp range 271–273 °C.

2.1.10. Synthesis of compound 13 (ethyl 4-cyanopicolinate)

Commercially available isonicotinonitrile (3.1 g, 30 mmol) was combined with $FeSO_4 \times 7H_2O$ (25.0 g, 90 mmol), DCM (150 mL), water (24 mL) and H_2SO_4 (4.9 mL) under cooling (−5 °C, NaCl-ice mixture). In a second flask, a mixture comprising ethyl pyruvate (16 g, 135 mmol) and H_2O_2 30 % (10 g, 90 mmol) was generated under cooling at −5 °C. Subsequently, the second solution was added dropwise to the first solution under vivid stirring and stirred for additional 15 min. The reaction mixture was poured into ice water. After separation of the two layers, the aqueous phase was extracted twice with DCM. Combined organic phases were dried over Na_2SO_4 and evaporated under reduced pressure. The resulting liquid crystallized overnight at room temperature. Finally, the solid was washed with well-chilled diethyl ether to yield a colorless solid (2.8 g, 53 %). ^{1}H NMR ($CDCl_3$): δ ppm = 1.47 (t, 3H, J = 7.2 Hz), 4.52 (q, 2H, J = 7.2 Hz), 7.72 (d, 1H, J = 4.8 Hz), 8.35 (s, 1H), 8.96 (d, 1H, J = 4.8 Hz); ^{13}C NMR ($CDCl_3$): δ ppm = 14.4, 62.9, 115.8, 122.0, 126.9, 128.2, 149.8, 151.0, 163.7; FTIR ($\tilde{\nu}$): 2241 (w), 1715 (s) cm^{-1}. mp range: 89–91 °C (89–93 °C) [33].

2.1.11. Synthesis of compound 14 (4-(1H-tetrazol-5-yl)picolinic acid ethyl ester)

4-Cyanopicolinic acid ethyl ester (**13**, 3.0 g, 17 mmol) was dissolved in toluene (50 mL). NaN_3 (1.4 g, 22 mmol) and triethyl amine hydrochloride (3.0 g, 22 mmol) were added, and the resulting mixture was stirred at 110 °C. After 16 h, the mixture was concentrated under reduced pressure and treated with aqueous sodium hydroxide solution until a pH of 12 was reached. The aqueous phase was washed three times with EtOAc and subsequently acidified with hydrochloric acid (36 %), resulting in precipitation of 4-(1*H*-tetrazol-5-yl)picolinic acid ethyl ester (**14**). The collected precipitate was washed with 2-propanol and dried to afford a colorless amorphous powder (3.261 g, 88 % yield). ^{1}H NMR (DMSO-d_6): δ ppm = 1.38 (t, 3H, J = 7.2), 4.42 (q, 2H, J = 7.2 Hz), 8.24 (d, 1H, J = 4.8 Hz), 8.64 (s, 1H), 8.96 (d, 1H, ^3J = 5.2 Hz); ^{13}C NMR (DMSO-d_6): δ = 14.8, 61.6, 121.6, 124.0, 133.5, 148.9, 151.1, 155.0, 164.1; FTIR ($\tilde{\nu}$): 1724 (s), 1610 (s) cm^{-1}. HRMS (ESI): calcd for $C_9H_{10}N_5O_2$ $[M + H]^+$ m/z, 220.0829; found m/z, 220.0818; mp range: 251–252 °C (decomposition).

2.1.12. Synthesis of compound 15 (4-(1H-tetrazol-5-yl)picolinic acid)

4-(1*H*-Tetrazol-5-yl)picolinic acid ethyl ester (**14**) (500 mg, 2.3 mmol) was suspended in MeOH (10 mL). An aqueous NaOH (365 mg, 9.2 mmol in 10 mL) solution was added and the resulting mixture was heated to reflux for 3 h. Upon acidification with hydrochloric acid (36 %), 4-(1*H*-tetrazol-5-yl)picolinic acid (**15**) precipitated, was collected by filtration and washed with aqueous MeOH (MeOH/water, 50:50, v/v) and dried to afford colorless crystals (411 mg, 94 % yield). ^{1}H NMR (DMSO-d_6): δ ppm = ^{1}H NMR (DMSO-d_6): δ ppm = 8.23 (d, 1H, J = 4.8 Hz), 8.65 (s, 1H), 8.96 (d, 1H, J = 4.8 Hz); ^{13}C NMR (DMSO-d_6): δ ppm = 121.6, 123.7, 133.5, 149.7, 150.9, 155.0, 165.6; FTIR ($\tilde{\nu}$): 3352 (m, $\nu_{O\text{-}H}$), 1722 (m, $\nu_{C=O}$), 1630 (s, $\nu_{C=N}$) cm^{-1}. HRMS (ESI): calcd for $C_7H_6N_5O_2$ $[M + H]^+$ m/z, 192.0516; found m/z, 192.0518; mp range 255–257 °C (decomposition).

2.1.13. Synthesis of compound 16 ((2R,S)-amino-2-(1H-tetrazol-5-yl) acetic acid ethyl ester hydrochloride)

Ethyl 2-(hydroxyimino)-2-(1*H*-tetrazol-5-yl)acetate (2.0 g. 10.8 mmol, 1.0 eq), prepared as described from commercially available oxyma (ethyl (*E*)-2-cyano-2-(hydroxyimino)acetate) [34]) was transferred into a two-neck flask which was evacuated and flushed with argon. $Pd(OH)_2$/C (200 mg) and ethanol (50 mL) were added to the flask. Subsequently, the installation was set under hydrogen atmosphere and stirred for 2 h at room temperature. Concentrated hydrochloric acid (1.8 mL) was added through a septum, and the reaction mixture was allowed to stir for an additional time of 24 h at room temperature. The catalyst was removed by filtration through diatomaceous earth. The volume of the resulting solution was decreased under reduced pressure to achieve precipitation. After a couple of hours, the solid was filtered off and washed with diethyl ether. Yield: quantitative (2.24 g); beige-colored solid; ^{1}H NMR (DMSO-d_6): δ ppm = 1.16–1.19 (t, 3H, J = 7.2 Hz), 4.21–4.29 (q, 2H, J = 7.2 Hz), 5.87 (s, 1H); ^{13}C NMR (DMSO-d_6): δ ppm = 13.8, 47.1, 63.0, 153.6, 165.2. FTIR ($\tilde{\nu}$): 1734 (s) cm^{-1}. HRMS (ESI): calcd for $C_5H_8N_5O_2$ $[M - H]^-$ m/z, 170.0683; found: m/z 170.0678; mp range 142–146 °C.

2.1.14. Synthesis of compound 17 ((2R,S)-4-bromobenzamido-2-(1H-tetrazol-5-yl)acetic acid ethyl ester)

(2*R*,*S*)-Amino-2-(1*H*-tetrazol-5-yl) acetic acid ethyl ester hydrochloride (**16**, 1.00 g, 4.8 mmol, described in Ref. [35]), pyridine (1.14 g, 14.5 mmol), and 4-bromobenzoyl chloride (1.38 g, 5.76 mmol) were suspended in acetonitrile (50 mL) and stirred in a round-bottom flask. The resulting solution was allowed to stir at room temperature for 1 h. After thin layer chromatography showed completion of the reaction, volatiles were removed by means of a rotary evaporator. The liquid residue was dissolved in a mixture of water and EtOAc (100 mL) and brine (100 mL) and extracted three times with brine (100 mL each) by means of a separation funnel. The combined organic phases were dried over anhydrous $MgSO_4$. After the spent drying agent was removed by filtration, the solvent was evaporated *in vacuo* to yield a colorless solid that was washed multiple times with hot cyclohexane. Drying under reduced pressure at elevated temperature (60 °C) for 24 h afforded a colorless solid (940 mg, 55 %). The product was recrystallized from water and dried for 24 h at reduced pressure and elevated temperature (50–60 °C) to determine the melting range. ^{1}H NMR (DMSO-d_6): δ ppm = 1.19–1.22 (t, 3H, J = 7.2 Hz), 4.20–4.26 (q, 2H, J = 7.2 Hz), 6.11 (d, 1H, J = 7.2 Hz), 7.73 (d, 2H), 7.87 (d, 2H), 9.73 (d, 1H, J = 7.2 Hz); ^{13}C NMR (DMSO-d_6): δ ppm = 13.9, 48.2, 61.9, 125.9, 129.8, 131.5, 131.9, 165.7, 167.1; FTIR ($\tilde{\nu}$): 1635 (s, $\nu_{C=O)}$, 1745 (s, $\nu_{C=O)}$ cm^{-1}. HRMS (ESI): calcd for $C_{12}H_{11}N_5O_3Br$ $[M - H]^-$ m/z, 352.0051; found m/z, 352.0034; mp range 180–181 °C.

2.1.15. Synthesis of compound 18 (4-bromo-N-{(1R,S)-2-[(2E/Z)-2-(1-methylpropylidene) hydrazino]-2-oxo-1-(1H-tetrazol-5-yl)ethyl] benzamide)

(2*R*,*S*)-4-Bromobenzamido-2-(1*H*-tetrazol-5-yl)acetic acid ethyl ester **17** (772 mg, 2.0 mmol) was dissolved in EtOH (50 mL) denatured with butanone (1 %) in a round-bottom flask, combined with an aqueous solution of hydrazine hydrate (3.76 mL (3.87 g) 80 % H_2N–NH_2·H_2O, 60.4 mmol), and stirred for 4 h under reflux. Subsequently, the mixture was stirred for 16 h at room temperature. After completion of the reaction, solvents were removed *in vacuo*. Residual hydrazine and water were removed by multiple azeotropic drying with EtOH. The resulting solid was filtered over a G4 glass filter funnel, washed with EtOH, and dried for 18 h at 8 mbar and 60 °C to yield a colorless solid (250 mg, 36 %) that was crystallized from 2-propanol/diethyl ether for melting point analysis. ^{1}H NMR (DMSO-d_6): δ ppm = 0.69–0.73/1.03–1.06 (t, 3H,

CH_3, $^3J = 7.2$ Hz), 1.80/1.88 (s, 3H, CH_3), 2.04–2.08/2.27–2.28 (m, 2H, CH_2), 6.27/6.66 (d, 1H, CH, $^3J = 7.2$ Hz), 7.69–7.73 (m, 2H, 2 × CH), 7.88–7.92 (m, 2H, 2 × CH), 9.34/9.49 (d, 1H, NH, $^3J = 7.6$ Hz), 10.66/10.73/10.80 (s, 1H, NH). ^{13}C NMR (DMSO-d_6): δ ppm = 9.9/10.7, 16.2/16.3, 31.1/31.5, 46.1/48.1, 129.9, 131.4 (2 × C13), 133.4, 155.1/161.4, 162.4/165.5, 165.8/167.5. FTIR ($\tilde{\nu}$): 1636 (s, $\nu_{C=O}$), 1691 (s, $\nu_{C=O}$) cm^{-1}. HRMS (ESI): calcd for $C_{14}H_{15}N_7O_2Br$ [M − H]$^-$ *m/z*, 392.0476; found *m/z*, 392.0491; mp range 211–214 °C.

2.1.16. Synthesis of compound 19 ((2R,S)-(5-phenylvaleramido)-2-(1H-tetrazol-5-yl)acetic acid ethyl ester)

2-Amino-2-(1*H*-tetrazol-5-yl) acetic acid ethyl ester hydrochloride (**16**, 1.00 g, 4.8 mmol), pyridine (1.17 mL, 1,15 g, 14,5 mmol), and 5-phenylpentanoyl chloride (1,89 g, 9,6 mmol) in acetonitrile (100 mL) were stirred in a round-bottom flask. After reaction completion, indicated by TLC analysis, solvents were removed by means of a rotary evaporator. The liquid residue was treated with EtOAc (100 mL) and brine (100 mL) and extracted three times with brine (100 mL each) by means of a separation funnel. The organic phase was dried over anhydrous $MgSO_4$. After the spent drying agent was removed by filtration, the solvent was evaporated *in vacuo* to yield a pale yellow solid that was washed multiple times with hot cyclohexane. Drying under reduced pressure at elevated temperature (60 °C) for 18 h afforded a pale yellow solid (1.17 g, 73 %). ^{1}H NMR (DMSO-d_6): δ ppm = 1.15 (t, 3H, $J = 7.2$ Hz), 1.53–1.55 (m, 4H), 2.22–2.25 (m, 2H), 2.55–2.58 (m, 2H), 4.16 (q, 2H, $J = 7.2$ Hz), 5.91 (d, 1H, $J = 7.6$ Hz), 7.14–7.18 (m, 3H), 7.25–7.28 (m, 2H), 9.05 (d, 1H, $J = 7.6$ Hz); ^{13}C NMR (DMSO-d_6): δ ppm = 13.7, 24.5, 30.3, 34.3, 34.8, 47.1, 61.6, 125.4, 128.0, 141.9, 167.1, 172.5; FTIR ($\tilde{\nu}$): 1525 (w, $\nu_{C=C}$), 1657 (w, $\nu_{C=O}$), 1737 (w, $\nu_{C=O}$) cm^{-1}. HRMS (ESI): calcd for $C_{16}H_{20}N_5O_3$ [M − H]$^-$ *m/z*, 330.1572; found *m/z*, 330.1581; mp range 118–119 °C.

2.1.17. Synthesis of compound 20 ((R,S)–N-{2-oxo-2-[2-(propan-2-ylidene)hydrazinyl]-1-(1H-tetrazol-5-yl)ethyl}-5-phenylvaleramide)

2-(5-Phenylvaleramido)-2-(1*H*-tetrazol-5-yl)acetic acid ethyl ester (**19**, 0.50 g, 1.5 mmol) was dissolved in EtOH (50 mL) in a round-bottom flask, combined with an aqueous solution of hydrazine hydrate (3.76 mL (3.87 g) 80 % H_2N–NH_2·H_2O, 60.4 mmol), and stirred for 4 h at 78 °C under reflux. After addition of acetone (5 mL), stirring under reflux was continued for further 2 h. Subsequently, the mixture was stirred for 16 h at room temperature. After completion of the reaction, solvents were removed *in vacuo*. Residual hydrazine and water were removed by multiple azeotropic drying with EtOH. The resulting solid was filtered over a G4 glass filter funnel, washed with EtOH, and dried for 18 h at 8 mbar and 60 °C to yield a pale yellow solid (0.23 g, 43 %). ^{1}H NMR (DMSO-d_6): δ ppm = 1.51–1.54 (m, 4H, CH_2, CH_2), 1.75–1.95 (m, 6H, 2 × CH_3), 2.22–2.28 (m, 2H, CH_2), 2.55–2.57 (m, 2H, CH_2), 6.08/6.49 (d, 1H, CH, $^3J = 7.6$ Hz/8.0 Hz), 7.14–7.19 (m, 3H, 3 × CH), 7.24–7.28 (m, 2H, 2 × CH), 8.70/8.80 (d, 1H, NH, $^3J = 8.0$ Hz/7.6 Hz), 10.58/10.61 (s, 1H, NH). ^{13}C NMR (DMSO-d_6): δ ppm = 17.0/17.7, 24.6/24.7/24.9, 30.3/30.5/32.3, 44.8/47.2, 125.6, 128.2, 128.3, 142.1, 151.9, 158.0, 167.4, 172.5. FTIR: $\tilde{\nu}$ = 1520 (w, $\nu_{C=C}$), 1650 (m, $\delta_{N\text{-}H}$), 1687 (w, $\nu_{C=O}$) cm^{-1}. HRMS (ESI): calcd for $C_{17}H_{22}N_7O_2$ [M − H]$^-$ *m/z*, 356.1840; found *m/z*, 356.1830; mp range 161–167 °C.

2.1.18. Protein expression, production, and crystallization

The pQTEV expression vector encoding the catalytic domain of human KDM4D (residues 1–342) was used to produce protein with an N-terminal His_6-tag. The protein was purified by means of metal affinity chromatography using binding buffer consisting of 50 mM HEPES pH 7.5, 500 mM NaCl, 20 mM imidazole, and 1 mM TCEP. The protein was eluted from resins using buffer consisting of 50 mM HEPES pH 7.5, 500 mM NaCl, 300 mM imidazole, and 1 mM TCEP. For the purpose of affinity tests and crystallization, the N-terminal affinity tag was removed by TEV protease. As a final stage of purification, the protein sample was subjected to size-exclusion chromatography in the following buffer: 10 mM HEPES pH 7.5, 200 mM NaCl, 5 % (v/v) glycerol, and 1 mM TCEP. Crystals were grown using the sitting-drop vapor-diffusion method at 291 K. The well solution consisted of 24 % (w/v) polyethylene glycol (PEG-3350), 180 mM ammonium sulfate, and 0.1 M HEPES buffer pH 7.0 and was mixed with approx. 19 mg/mL protein solution. A Gryphon crystallization robot (Art Robbins Instruments) was used to mix equal volumes of 0.4 mL of protein and well solution on a 96-well low-profile Intelli-Plate (Art Robbins Instruments). Regular tetragonal bipyramid crystals appeared after 2 days and grew to a maximum length of 150 μm within a week.

2.1.19. X-ray diffraction data collection, processing, structure determination, and refinement

For preparation of protein-ligand complexes, crystals were pre-soaked in well solution supplemented with 10 mM $NiCl_2$ for 10 min. Subsequently, crystals were transferred to the ligand-soaking solution, consisting of 100–150 mM ligand mixed with the well solution and 10–15 % (v/v) final DMSO concentration. Most ligands were soaked for 24 h (compounds **5–10)**; however, based on the visual inspection and diffracting power, some soaking experiments were performed more rapidly. Only 1 min of soaking was used for compound **1**, 5 min for compound **4**, 30 min for compound **3**, and 12 h for compound **2**. The crystals were flash-cooled in liquid nitrogen [36] following cryo-protection by quickly immersing them in well solution complemented with 20 % (v/v) ethylene glycol. Diffraction data were collected on beamlines BL14.1 and BL14.2 at wavelength 0.9184 Å at the BESSY II electron storage ring operated by the Helmholtz-Zentrum Berlin [37] by using a PILATUS detector. X-ray data were integrated and scaled using XDSAPP [38]. All relevant data collection and processing statistics are given in Table 1. The structures were solved in space group $P4_32_12$ by molecular replacement using the program Phaser [39] using the structure with the PDB-Id 6ETV [27] as a search model. The preliminary models were initially refined with REFMAC [40,41]. Later, after several cycles of manual model correction in COOT [42] and refinement with phenix.refine [43] the structures were validated. Atomic coordinates and corresponding structure factor amplitudes were deposited in the Protein Data Bank. Refinement statistics are summarized in Table 2.

2.1.20. ITC measurements

ITC measurements on KDM4D and the respective tetrazolylhydrazide ligands were performed using a MicroCal PEAQ-ITC microcalorimeter (Malvern Panalytical GmbH, Germany). Experiments were performed in 10 mM HEPES buffer at pH 7.5, 0.5 M NaCl, 5 % (v/v) glycerol, and 1 mM TCEP at 20 °C. The protein concentration was determined spectrophotometrically at λ = 280 nm by using the calculated molar extinction coefficient. The tetrazole ligands were diluted 100–250 times in buffer up to the working concentration from stock solutions in DMSO. The DMSO concentration in the resulting solutions ranged from 0.4 to 1 %. Solutions of KDM4D were supplemented with the corresponding amount of DMSO to avoid thermal effects due to buffer mismatch. Tetrazole ligands were titrated in 13 or 19 steps (2–3 μL) into a protein solution in the calorimeter cell. Other experimental settings included a spacing time of 180 s and a filtering period of 5 s. For each ligand, measurements were performed two or three times. For all experiments, the instrument software (MicroCal PEAQ-ITC Analysis) was used for baseline adjustment, peak integration, and normalization of the reaction heats, with respect to the molar amount of injected ligand, as well as for data fitting and binding parameter evaluation.

3. Results

3.1. Compound design considerations and chemical synthesis

For the study focusing on mapping the distal histone binding pocket, we decided to use the ligand architectures that consist of stable core motifs linked with versatile extensions. The cores of the compounds are

Table 1
Data collection and processing statistics. The values in parentheses are for the respective highest-resolution shell.

Compound	1	2	3	4	5	6	7	8	9	10
BESSY beamline	BL14.2	BL14.1	BL14.1	BL14.1	BL14.1	BL14.1	BL14.1	BL14.1	BL14.1	BL14.1
Detector	Pilatus 3 2 M	Pilatus 6 M	Pilatus 6 M	Pilatus 6 M	Pilatus 6 M	Pilatus 6 M	Pilatus 6 M	Pilatus 6 M	Pilatus 6 M	Pilatus 6 M
Crystal-detector distance (mm)	144	180.8	239.3	267.2	180.8	210.7	180.8	149.2	181.2	149.2
Total rotation range (°)/frames	150/1500	150/1500	150/1500	100/1000	180/1800	150/1500	180/1800	180/1800	180/1800	180/1800
Exposure time										
Resolution range (Å)	48.38–1.6 (1.7–1.6)	48.53–1.43 (1.51–1.43)	48.44–1.48 (1.56–1.47)	48.41–1.58 (1.67–1.58)	48.2–1.51 (1.61–1.51)	48.2–1.64 (1.74–1.64)	48–1.21 (1.29–1.21)	47.92–1.23 (1.3–1.23)	48.2–1.34 (1.42–1.34)	47.9–1.1 (1.17–1.1)
Space group	$P4_3\,2_1\,2$									
Unit cell a, c (Å)	72.15,152.39	72.47,151.67	72.08 151.59	72.21,152.08	71.93,151.18	71.88,150.95	71.55,150.74	71.48,150.71	71.90,151.25	71.45,150.69
Mosaicity (°)	0.291	0.066	0.186	0.230	0.145	0.272	0.102	0.104	0.118	0.050
Total no. of reflections	564,060 (84,437)	823,152 (129,611)	745,443 (120,061)	397,773 (64,204)	769,613 (127,441)	495,957 (83,237)	1,540,341 (244,631)	1,484,777 (237,653)	1,148,877 (170,965)	2,025,426 (319,687)
No. of unique reflections	99,966 (15,546)	143,054 (22,737)	130,066 (20,919)	104,082 (16,734)	114,697 (18,843)	48,623 (7673)	226,689 (36,392)	216,345 (34,865)	169,112 (26,862)	292,411 (46,319)
Multiplicity	5.64	5.75	5.73	3.82	6.71	10.20	6.79	6.86	6.79	6.92
Completeness (%)	99.2 (95.6)	99.6 (97.8)	99.9 (99.4)	98.5 (97.8)	97.3 (98.8)	98.6 (98.5)	99.8 (99.1)	99.9 (99.5)	99.4 (97.7)	97.6 (95.4)
Mean I/σ(I)	12.54 (0.64)	13.1 (0.88)	11.15 (0.66)	10.31 (0.51)	16.55 (2.12)	14.23 (1.99)	17.13 (1.83)	18.69 (1.95)	18.42 (1.87)	16.52 (1.98)
R_{meas} (%)	9.4 (259.4)	9.9 (197.8)	10.3 (246.4)	9.3 (315.9)	10.8 (96.9)	16.7 (119.7)	6.4 (104.4)	6.6 (105.3)	7.3 (98.5)	6.4 (99.9)
$CC_{1/2}$	99.9 (21.5)	99.9 (35.5)	99.9 (25.2)	99.9 (24.6)	99.9 (76.1)	99.8 (72.3)	100.0 (66.7)	100.0 (68.8)	100.0 (67.7)	100.0 (70.7)
ISa	26.51	29.01	27.66	32.14	40.62	28.52	30.56	38.37	41.24	33.24
Wilson B factor ($Å^2$)	26.4	17.3	22.8	25.4	12.2	14.9	12.3	11.8	12.7	10.8

examples of scaffolds known to bind to the 2OG-binding site: nicotinic acid and tetrazolylhydrazides. In addition, combinations of both nicotinic acid and tetrazoles were designed and synthesized. The extensions are mainly flexible tails with varying lengths and chemical properties. They are designed to probe the histone-binding cavity to detect possible additional interactions within the distal area. The ten compounds discussed in the study are listed in Fig. 1. Compounds 1–4 possess a nicotinic acid scaffold. The pyridine N atom coordinates the active site metal cation, while the carboxylic acid in position 4 forms hydrogen bonds, mimicking those of 2OG, with Tyr and Lys residues [24]. A direct connection between an amine and the pyridine ring in position 3 was reported to lead to nanomolar inhibition [26]. Compounds 3–10 (Fig. 1) possess a tetrazolylhydrazide scaffold, the binding mode of which, as a competitor for the natural KDM4 cofactor, has been described previously [27].

3.1.1. *Synthesis of compounds 1 and 2*

To explore new KDM-ligand interactions, compounds **1** and **2** were designed to have an amine coupled to position 2 of the isonicotinic ring. They were then synthesized from 2-chloro-isonicotinic acid (**11**) by nucleophilic displacement of the activated chloro-substituent adjacent to the pyridine N-atom at position 2 with either 3-aminopropan-1-ol yielding new target compound **1**, or ethylene diamine, yielding known analog **12** [44] (Scheme 1). The hydrochloride **12** was subsequently transformed into the corresponding free base *in situ* and acylated with methanesulfonyl chloride to yield the new sulfonamide **2**.

Reagents and conditions: (a) 3-aminopropan-1-ol, neat, 120 °C, 22 h (26 %); (b) ethylene diamine, μW, 1 h, 180 °C (72 %); (c) NaOH, water, methanesulfonyl chloride, 0 °C, 4 h; room temp. 20 h (29 %).

3.1.2. *Synthesis of compounds 3 and 4*

For compounds 3 and 4, in particular, the tetrazole group was introduced as a bioisostere replacement for the carboxylic acid of compounds 1 and 2. Combining the tetrazole group and the pyridine rings leads to an enlarged conjugated aromatic system. Moreover, in **3** and **4**, a carbonyl function in position 2 of the pyridine ring was added to address the catalytic center with a possible chelating moiety comprising the carbonyl O- and pyridine N-atom. Target compounds **3** and **4** were synthesized from commercially available 4-cyanopicolinic acid ethyl ester (**13**). The tetrazole ring of these compounds was built up by the known reaction of the cyano group with hazardous hydrazoic acid generated slowly and in minute amounts *in situ* from sodium azide (Scheme 2). The resulting intermediate **14** could be transformed to **3** by aminolysis using 3-morpholinopropylamine under microwave irradiation. Hydrolysis of ester **14** with sodium hydroxide afforded the carboxylic acid **15**, which could be activated via the corresponding acid chloride (not shown) by means of oxalyl chloride. This intermediate was not isolated but quenched with hydroxylamine liberated *in situ* to yield hydroxamic acid **4**.

Reagents and conditions: (a) NaN_3, $(C_2H_5)_3N{\cdot}HCl$, toluene, 110 °C, 16 h (88 %); (b) 3-morpholinopropylamine, neat, μW, 45 min, 165 °C (18 %); (c) NaOH, water, MeOH, reflux, 3 h, (94 %); (d) oxalyl chloride, DMF, 0 °C; $NH_2OH{\cdot}HCl$, DIPEA (21 %).

3.1.3. *Synthesis of compounds 5 and 6*

Compounds **5** and **6** were synthesized from known 2-amino-2-(1*H*-tetrazol-5-yl) acetic acid ethyl ester hydrochloride (**16**) [35] as depicted in Scheme 3. While **5** and **6** could be synthesized from starting material **16** in two steps *via* intermediates **17** and **19**, respectively, the products obtained were sticky and hygroscopic, and a synthetic deviation was necessary to obtain the target compounds analytically pure. It was discovered by chance that treatment of **17** with hydrazine in the presence of butanone (stemming from denatured ethanol), a hydrazone derivative **18** was obtained as a side-product that could be converted to analytically pure target compound **5**. Because this unintentionally formed hydrazone **18** consists of a mixture of four stereoisomers due to

Table 2
Refinement and validation statistics.

Compound	1	2	3	4	5	6	7	8	9	10
Refinement program	Refmac5 & Phenix.refine									
Resolution (Å)	29.41–1.61	48.53–1.43	48.44–1.48	48.41–1.58	42.2–1.52	48.17–1.64	48–1.21	35.7–1.23	42.2–1.34	35.73–1.1
Reflections in working set	97,726	140,606	126,626	101,712	111,013	46,491	224,315	214,044	167,034	289,319
Reflections in test set	2094	2095	2094	2101	2067	2099	2374	2287	2072	3080
R_{work} (%)	16.7	14.3	16.1	17.8	19.1	18.2	12.4	12.0	12.9	12.3
R_{free} (%)	19.2	17.4	18.3	19.8	22.2	21.8	15.8	13.6	15.1	13.3
Number of non-H atoms	3152	3437	3259	3191	3358	3252	3497	3547	3523	3662
macromolecule	2747	2897	2815	2778	2846	2756	2997	2967	2972	3060
ligands	63	66	61	79	43	38	64	101	58	96
water	342	475	383	334	469	458	436	479	493	506
RMS (bonds) (Å)	0.012	0.010	0.08	0.015	0.006	0.007	0.016	0.01	0.009	0.012
RMS (angles) (°)	1.106	1.138	1.029	1.339	0.946	1.027	1.563	1.165	1.237	1.491
Ramachandran favored (%)	99	99	99	99	99	98	100	99	98	100
Clashscore	0.72	3.23	2.65	1.78	1.74	3.64	6.86	4.10	5.66	8.84
Average B factor (Å^2)	32.4	22.3	34.4	31.9	19.72	20.96	18.9	18.49	19	17.46
Ligand occupancy	1	1	0.77	1	1	1	0.65	0.25/0.25/0.5	0.69/0.74	0.78/0.8
PDB ID	6F5R	6F5Q	6F5S	6F5T	6H11	6H0X	6H0Y	6H0W	6H0Z	6H10

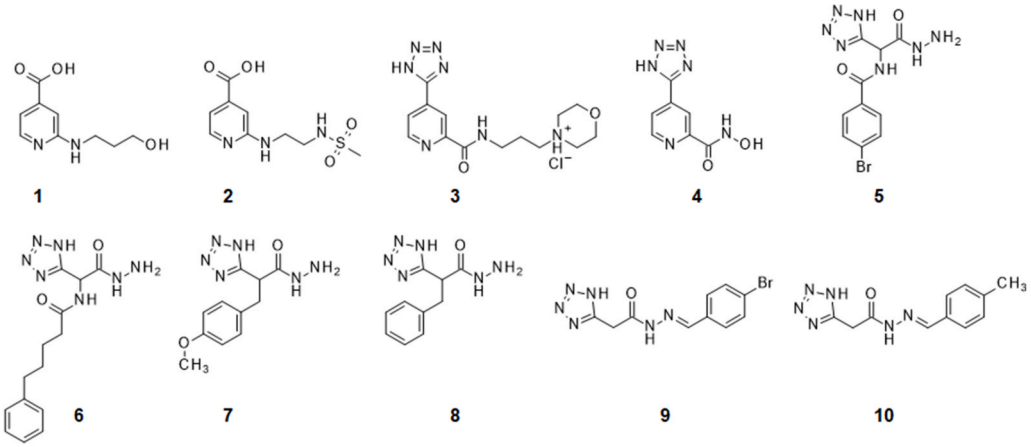

Fig. 1. Chemical structures of compounds **1–10**, which were used for soaking into KDM4D crystals.

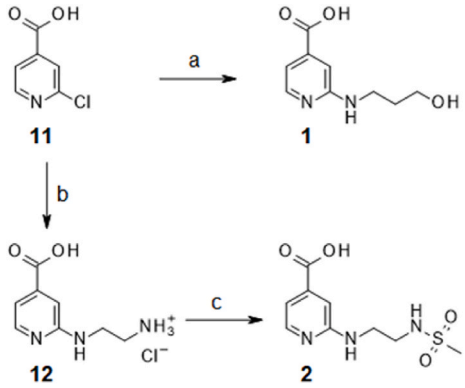

Scheme 1. Synthesis of target compounds **1** and **2**.

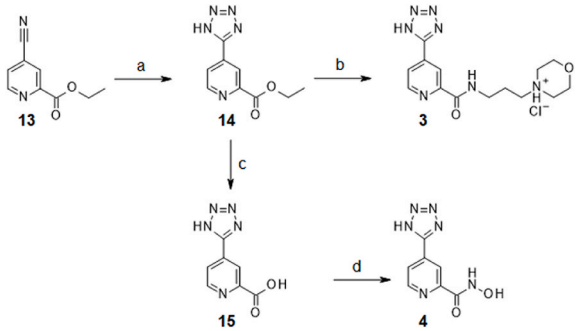

Scheme 2. Synthesis of target compounds **3** and **4**.

the presence of a chiral center plus an unsymmetrically substituted double bond, giving rise to *E* and *Z*-isomers, the transformation of **19** to **6** *via* an intermediate hydrazone was simplified by adding the symmetrical ketone acetone as a replacement for butanone. The racemic reaction product **20** could be isolated in moderate yield and led to less crowded NMR spectra compared to the diastereomeric mixture **18**. Both intermediates **18** and **20** were treated with aqueous ammonia in order to obtain the two racemic compounds **5** and **6**, respectively, analytically pure and in a less hygroscopic form, albeit in low or even very low yield, respectively.

Reagents and conditions: (a) 4-bromobenzoyl chloride, pyridine, acetonitrile, room temp. (55 %); (b) EtOH with 1 % butanone, $H_2N–NH_2·H_2O$, water, 4 h, reflux; 16 h room temp. (36 %); (c) water, NH_3, EtOH, 5 h, reflux (6 %) (d) 5-phenylpentanoyl chloride, pyridine, acetonitrile, room temp. (73 %); (e) $H_2N–NH_2·H_2O$, water, EtOH, 4 h, 78 °C; acetone, 2 h, reflux (43 %); (f) water, NH_3, EtOH, 5 h, reflux (6 %).

3.1.4. Synthesis of compounds 7-10

The synthesis of the racemic Knoevenagel products **7** and **8**, which also contain the hydrazide and tetrazole functions [31], as well as of the related hydrazones **9** and **10** was carried out as published [28].

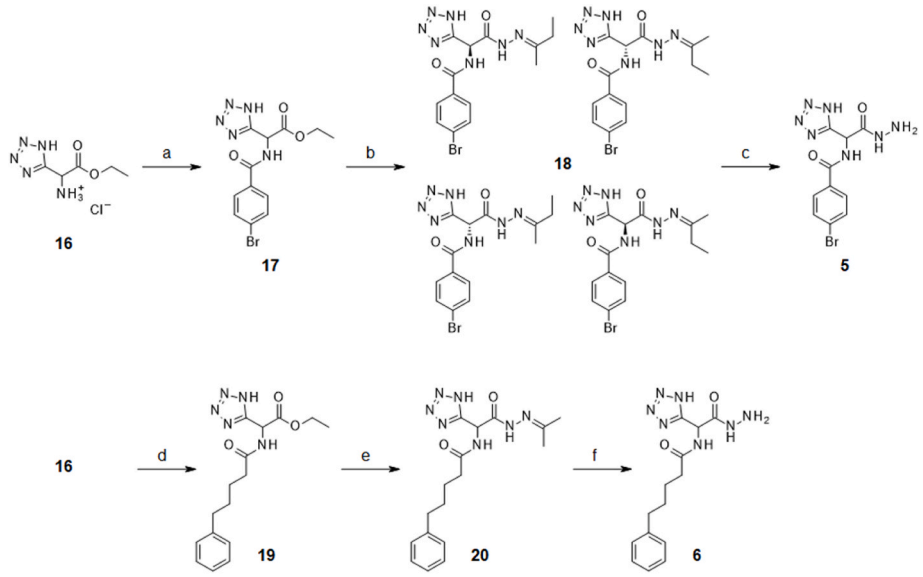

Scheme 3. Synthesis of target compounds **5** and **6**.

3.2. Structural investigations

All structural studies described here were carried out using the KDM4D enzyme. KDM4D is a suitable representative of the KDM4 subfamily, and, as shown earlier [27] the overall rigidity, packing, and quality of the tetragonal crystal form of KDM4D provide a solid basis for ligand soaking experiments.

3.2.1. Overall structure of KDM4D

The structure of the KDM4D catalytic domain described in this study is within experimental error, identical to previously determined KDM4D structures [45]. As in other KDM4 subfamily members, it is globular and consists of two Jumonji (Jmj) domains. The N-terminal JmjN domain comprises residues 18–60, while the C-terminal JmjC domain comprises residues 146–312 (Fig. 2). In all structures determined so far, a metal ion is bound in a deep cleft in the enzyme's active site. Naturally occurring Fe^{2+} is replaced by stable and similar in size Ni^{2+} ions during crystal soaking.

3.2.2. Ligand structures (Supplementary Figure 1)

All structures describing KDM4D in complex with compounds **1–10** (Fig. 1) are crystal structures in which the ligand has been soaked into the KDM4D crystals. The resulting structures show that several ligands occupy the 2OG binding site, interacting with active site residues. Similar binding poses have been observed previously for shorter tetrazolylhydrazide ligands [27] or other cofactor-mimicking molecules such as isonicotinic acid derivatives [46]. In addition, some of the new ligands extend towards the entrance of the histone binding pocket and the methylated lysine binding site and exhibit further interactions with KDM4D that may be utilized to enhance binding affinity or selectivity.

3.2.2.1. Structure of KDM4D with compounds 1–4 (Fig. 3). This group of compounds represents molecules with an isonicotinic acid (**1** and **2**; Fig. 3a and **b**) and tetrazole (**3** and **4**; Fig. 3c and **d**), the carboxylic acid group bioisostere replacement. Clear electron density is observed for the cores of all ligands: the pyridine ring is sandwiched between the two aromatic active-site residues Tyr181 and Phe189 by π-stacking interactions. The N atom of the pyridine is placed opposite to the Glu194-O atom and binds to the active-site metal ion. The carboxylate group of the ligands **1** and **2** occupies the same position as its counterpart in the natural cofactor, maintaining interactions with Lys210-NZ and Tyr136-OH. In addition, the tetrazole rings of the ligands **3** and **4** are aligned almost co-planar with the pyridine ring and sandwiched between two aromatic active-site residues, Tyr181 and Phe189, taking part in the π-stacking interactions.

The N atom of the partially flexible ligands **1** and **2** tail interacts with His192-NE2, which is also a metal ion ligand. In the tail of ligand **1**, the electron density is weak, suggesting that the tail is flexible or occurs in several conformations. Thus, introducing this apparently flexible and hydrophobic part to the ligand appears to have no favorable effect on ligand-protein interactions, whereas in ligand **2** one of the oxygen atoms of the sulfonamide group is situated 2.9 Å from His90-NE2, suggesting the presence of a hydrogen bond. The other oxygen is 3.0 Å away from Ala190-N, also indicating the formation of a hydrogen bond. The carbonyl oxygen atom of the ligands **3** amide group is engaged in Ni^{2+} binding and interaction with Glu194-OE2. Again, the tail of this ligand exhibits weak electron density and does not interact with the protein. In the case of ligand **4**, the metal binding is bidentate and strengthened by a nitrogen atom of the hydroxamic group. The hydroxamic nitrogen atom also interacts with Glu194-OE2, which, at the same time, is a metal ion ligand. The bidentate rigid chelation motif causes the plane of the pyridine ring to twist by about 18° compared to the situation observed for compounds 1 and 2. Both oxygen atoms of the hydroxamic portion form hydrogen bonds with Lys245-NZ stabilizing the lysine side chain in one defined position.

3.2.2.2. Structure of KDM4D with compounds 5–8 (Fig. 4). This group of compounds represents molecules with a core motif that utilizes the hydrazide group to bind the metal ion in a bidentate mode. The nitrogen atom is positioned opposite the other metal ligand, His 280, while the oxygen atom binds opposite to Glu194. In the case of ligand **8** (Fig. 4d), apart from this predominant binding mode for the full-length ligand, its truncated versions are also observed in a low occupancy.

In ligands **5** (**Fig. 4a**) and **6** (Fig. 4b), the hydroxyl group of Tyr136 binds both the tetrazole ring in the 2OG binding site and additionally interacts with the amide nitrogen atom of the ligand tail in the histone binding site. The two-site binding stabilizes the position of the tyrosine side chain, which is observed here in a single conformation in contrast to the other structures. As in the previous group, the tetrazole ring of ligands **5** and **6** is sandwiched between two aromatic active-site residues, Tyr181 and Phe189. In addition, in the case of **5,** the other nitrogen in the tetrazole ring interacts with Asn202-OD1. The flexible tails of the ligands **5** and **6** points outward from the binding cleft and occupies the histone binding site inducing the movement of protein loop Ala 315-Ser

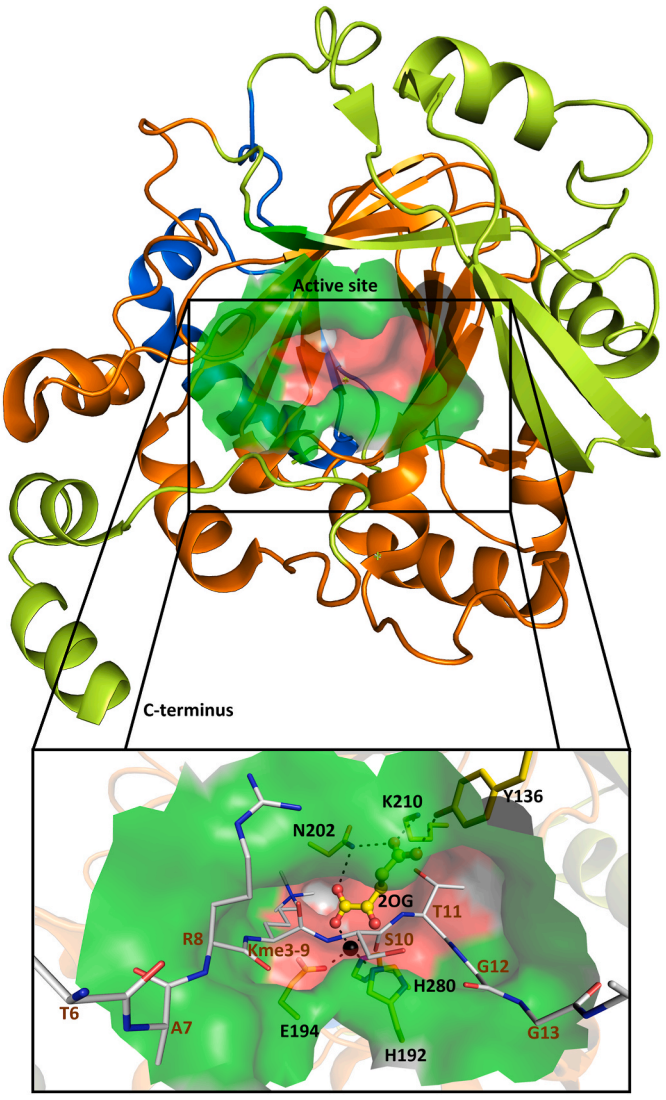

Fig. 2. The overall structure of KDM4D demethylase and its ligand binding site. The binding site is depicted as translucent surface; the catalytic and 2OG binding site is colored red, while the histone binding site is colored green. Top: Domain organization in KDM4D. The JmjN domain is colored blue, the C-terminal JmjC domain is green, the middle linking part is colored orange. Bottom: Zoom into the histone binding site. Relevant elements from the crystal structure PDB 4HON are emphasized. The KDM4D-bound cofactor 2OG is shown in ball-and-stick representation with carbon atoms in yellow, and the histone-derived peptide is given in silver stick representation with brown labels. Active-site residues are depicted as yellow sticks and labeled in black.

320. The ligands' **6** effect on the protein movement is even more pronounced. Herein, the phenyl ring points out toward the histone binding site and is sandwiched between His90 and Arg316, where it is held in place by stacking interactions (Fig. 6). The general rigidity of the ligand's **7** tail (Fig. 4c) makes the tetrazole ring interacts with the Lys210-NZ and Asn202-ND2 atoms but not with Tyr136-OH. The aromatic residues Phe189 and Tyr136 are both modeled with two alternative conformations. The oxygen of the ligand tail interacts with the amide nitrogen atom of Ala190. In the case of the **8**, the tetrazole ring protrudes towards the histone binding site, and its nitrogen atom interacts with Lys240-NZ.

3.2.2.3. Structures of KDM4D with compounds 9 and 10 (Fig. 5a and b). Both compounds, **9** and **10** (Fig. 1), have a very similar structure and are modeled in the same protein pocket, forming the same interactions with protein residues. Nitrogen atoms of the tetrazole ring form hydrogen bonds with the amide nitrogen atoms of Phe 287 and Thr112. The tetrazole ring occupies the position of the Gln 111 side chain, breaking its interaction with Asn 106, which points outwards into the solven. The ligand carbonyl oxygen interacts with Asn106-ND2. The amide nitrogen of the ligand binds to Glu208-OE2. At a distance of just 4.0 Å between the Leu206-CD2 atom and the center of the aromatic phenyl ring of the ligand, a CH-π hydrogen bond [47] is formed, contributing to ligand binding.

3.3. Ligand binding investigation by isothermal titration calorimetry (ITC)

To obtain quantitative values for the affinity and energetics of the ligand binding, complex formation was studied by ITC. In all cases, the ligand was titrated into the protein solution kept in the calorimeter cell. The thermodynamic parameters of ligand binding to KDM4 are presented in Table 3. The thermal effect of the binding was measurable only for four of the ten ligands. No clear signal could be detected for the remaining six, although all of them have been tested by ITC. The binding of the structurally similar compounds **1** and **2** is exothermic and characterized by an intermediate affinity, with dissociation constants (K_d) of 55.9 and 35.5 μM, respectively. For both compounds, enthalpic and entropic contributions (Table 3) make up the interaction, albeit the balance of these contributions is inverted. While for compound **2**, the enthalpic part dominates with nearly 80 % contribution to the Gibbs free energy of binding, for compound **1,** the entropic contribution plays a significant role in ligand binding, providing 70 % of the Gibbs free energy of interaction. The combination of pyridine, tetrazole, and hydroxamic moieties in the structure of compound **4** drastically increases the ligand affinity to KDM4D. With a K_d of 0.55 μM, it binds KDM4D two orders of magnitude stronger than compounds **1** and **2**. The binding of compound **4** is endothermic, and this strong interaction is favored solely by a substantial entropic contribution that overcompensates the unfavorable binding enthalpy. Replacement of the compact hydroxamic group with a long tail in compound **3** shows no ligand binding to KDM4D in an aqueous solution, and no binding isotherm could be recorded for this compound. In an aqueous buffer, compounds **5**, **7**, and **10** yielded similar results with no measurable binding to KDM4 at 20 °C. The interaction of compound **6** with KDM4D was endothermic, with a large unfavorable binding enthalpy. The large entropic contribution of binding cannot effectively overcompensate the positive enthalpy, which results in a relatively low affinity to KDM4 with a K_d of 0.5 mM.

4. Discussion

Given the known cellular functions of 2OG-dependent KDMs and their role in cancer initiation and progression, there is a great demand for potent, selective, and cell-permeable inhibitors. To extend the diversity of KDM-directed compounds, a set of molecules containing various KDM core binding scaffolds, ranging from known nicotinic acids to compounds bearing bioisosters of carboxylic moieties, tetrazole or hydrazide groups, have been assembled. By fusion of potent metal-ion binders with flexible and versatile moieties, the study presented here particularly emphasizes probing the histone binding site distal to the cofactor binding. This approach can be an alternative or supplement for the other structure-based approaches in drug discovery processes, such as fragment screening based on random protein-ligand structural information. Especially now, when technological advances at macromolecular crystallography beamlines are great, and access to synchrotron sites is easy.

Our ligands' binding modes have been elucidated through crystal structural analysis (Fig. 7). Preferred hot spots of binding have been analyzed as this information is of great importance to facilitate further optimization of binders in terms of affinity and selectivity. Compounds

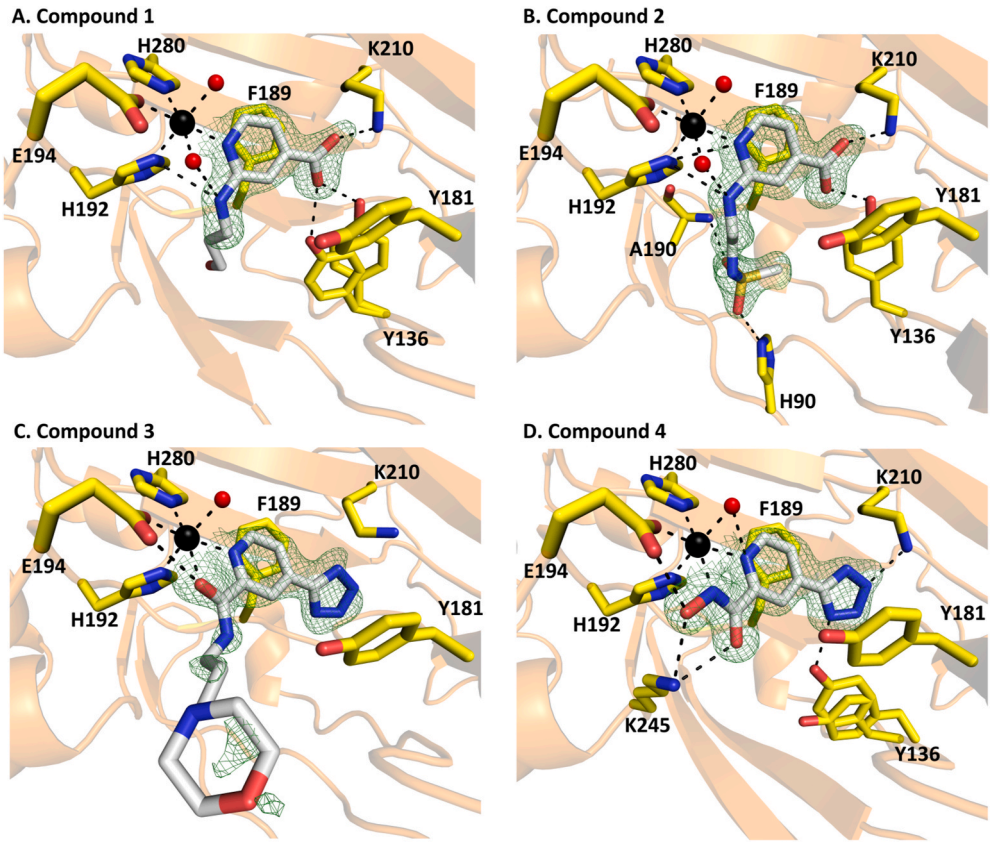

Fig. 3. Binding modes of the four pyridine-scaffold ligands in the KDM4D active site. Elements of the protein structure are depicted as semi-transparent orange ribbons, except for the side chains of the relevant amino acid residues, which are shown as yellow sticks. The presence of the ligand, also depicted as sticks, is evidenced by the 2mFo-DFc composite omit electron density map in green contoured at 1.2σ in panels A, B, D, and at 1 σ in panel C. Water molecules are shown as red spheres and the Ni^{2+} ion as a black sphere. The interactions between the ligand and the protein, water molecules, and metal ion are indicated as black dashed lines.

possessing an isonicotinic acid core (Fig. 3a/b), a scaffold present in many KDM inhibitors, were tested. This scaffold is at the core of the broad-spectrum 2OG oxygenase inhibitors such as pyridine-2,4-dicarboxylic acid (2,4-PDCA) and recently developed 3-amino-4-pyridine carboxylate derivatives [26]. Its metal binding capacity in the KDM active site is well-known and is mediated by a nitrogen atom of the pyridine ring. Molecules based on this scaffold were demonstrated to be excellent binders as they retain the natural 2OG cofactor interactions. It is worth noting that those interactions were identified as important in gaining affinity in most reported ligands. Thus, flexible tails of varying lengths were attached to the pyridine ring to map the binding potential far from the 2OG side. In the crystal structure of the KDM4D-bound compound **2**, two unique interactions within the histone binding site via His90-NZ and the peptide nitrogen of Ala190 were observed. Sulfonamide-mediated interactions of compound **2** contribute to increased affinity of the ligand in comparison with structurally very close compound **1,** which lacks these interactions and is characterized by nearly 40 % lower binding affinity (Table 3).

Tetrazole-containing compounds **3** and **4** were designed and synthesized to test further the concept of bioisosteric exchange (Fig. 3c and d). It was previously reported that substituting carboxylic acid with other moieties, in most cases, significantly lowers the potency or abolishes the binding of KDM4 inhibitors [46]. However, our study proves that such a substitution can be made while retaining satisfactory binding affinity. Interestingly, in most of the tetrazole-containing compounds from our screening, the native interactions of 2OG with Tyr136 and Lys210 are preserved. As the tetrazole ring is bulkier than a carboxylic group and requires more space, the movement of the Tyr136 side chain extending the 2OG binding pocket is observed upon its binding. In compound **4**, the most potent binder of this screening exhibiting sub-micromolar affinity, the hydroxamic group is observed to provide a second N-atom to assist the pyridine as a metal chelator (Fig. 3c). Additional affinity gain also arises from its two oxygens interacting with Lys245-NZ and Glu194-OE1. The saturation of hydrogen-bond interactions comprising metal and protein binding makes the hydroxamic group worth exploring further in the context of KDM inhibition. Compound **3**, with the same core scaffold and long tail but no hydroxamic acid, does not show preferable binding, and its binding affinity was not measurable. Notably, hydroxamic acid moieties were already employed in approved histone deacetylase targeting drugs like vorinostat, panobinostat, and belinostat [48], which usually work as bidentate metal chelating scaffolds. However, in the case of compound **4**, the bidentate metal ion chelation is mediated jointly by the hydroxamic acid and an N-atom from the pyridine ring, which is, to the best of our knowledge, the first time that such an interaction has been observed.

Another group of ligands, the tetrazolylhydrazides, were previously analyzed in terms of binding to KDM4 proteins [27,28]. Extending the tetrazolylhydrazide molecules by introducing flexible arms, additional binding spots in the histone binding site were explored. As anticipated, crystal structures showed that compounds **5–8** display a single predominant binding mode of the core structure to KDM4D. This binding mode is like one previously reported as ligand **6** [27]. However, compound **7** confirmed the hydrogen-bonding potential of the Ala190 peptide nitrogen with the ligand's ether oxygen, also observed in compound **2**.

In the cases of compounds **5** and **6**, a bidentate binding of Tyr136 by the tetrazole nitrogen and the amide group of the ligand's tail was observed. Moreover, in compound **6** an additional interaction in the histone binding pocket was gained as the ligand's carboxylate binds Lys245. In a crystal structure of a KDM4D-bound histone peptide, the

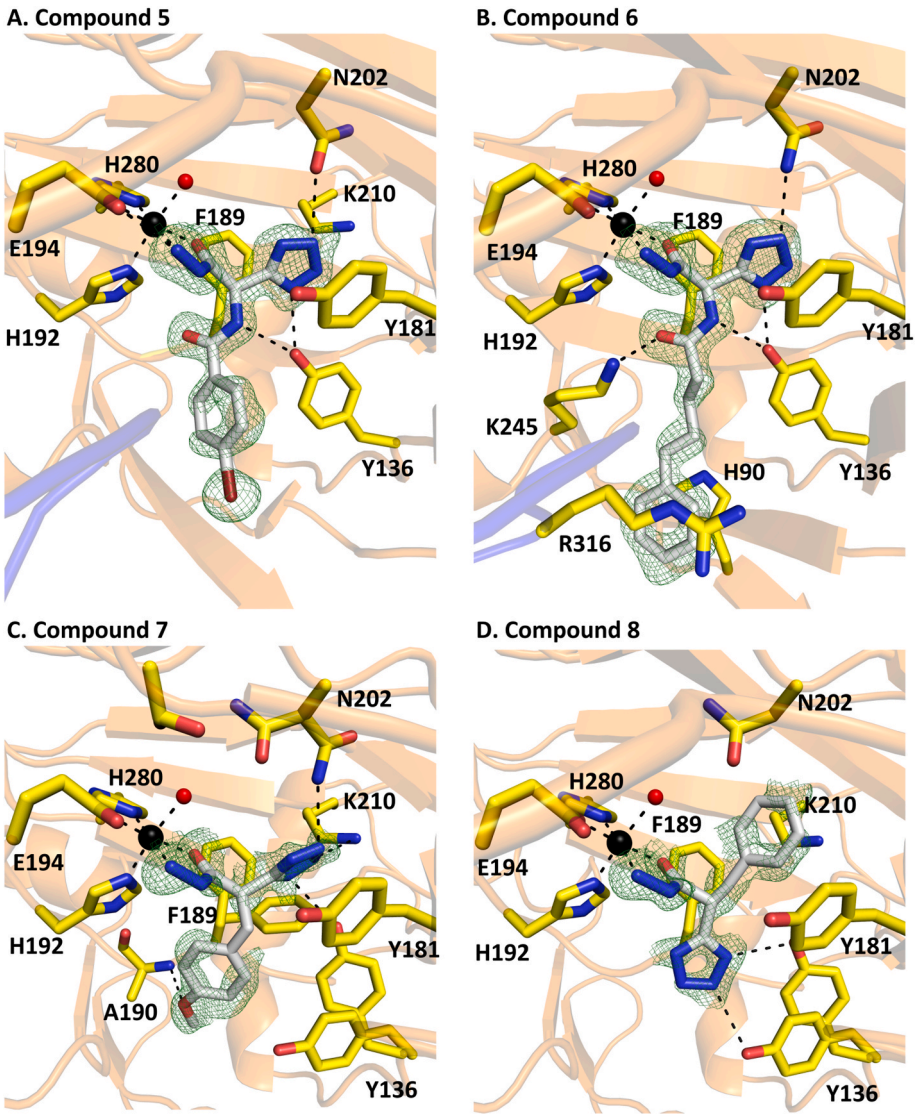

Fig. 4. Binding modes of the four tetrazolylhydrazide-scaffold ligands in the KDM4D active site. Elements of the protein structure are depicted as semi-transparent orange ribbons, except for the side chains of the relevant amino acid residues, which are shown as yellow sticks. The flexible loop is depicted as blue ribbon. The presence of the ligand, also depicted as sticks, is evidenced by the 2mFo-DFc composite omit electron density map in green contoured at 1.2σ in panel A and at 1 σ in panels B, C, and D. Water molecules are shown as red spheres and the Ni^{2+} ion as a black sphere. The interactions between the ligand and the protein, water molecules, and metal ion are indicated as black dashed lines.

Table 3
Thermodynamic parameters of ligand binding to KDM4D.

Compound	K_d (μM)	ΔH (kcal/mol)	$-T\Delta S$ (kcal/mol)	ΔG (kcal/mol)	N
1	55.90 ± 29.80	−1.65 ± 0.70	−4.05	−5.70	0.99
2	35.50 ± 5.90	−4.60 ± 0.50	−1.35	−5.97	0.97
4	0.55 ± 0.20	5.30 ± 0.20	−13.70	−8.40	0.80
6	509 ± 38	8.50 ± 0.40	−12.90	−4.42	1.00

very same lysine residue binds the carbonyl oxygen of histone's Ser10, which is next to the trimethylated lysine (K9me3) [45] (Fig. 2).

By comparing all of the presented crystal structures with that comprising a bound histone peptide, more potential spatial conflicts have been identified. The brominated ring of compound **5** occupies the space accommodating Thr11 of the KDM4D-bound histone peptide.

In addition to the steric overlaps between the KDM4D-bound histone peptide and our compounds, a narrowing of the histone binding site was also observed. In the crystal structure with compound **5**, a protein loop comprising Ala 315-Ser 320 undergoes a conformational change, making the histone binding cleft smaller by positioning Thr318 near the position of K9me3. In addition to the aforementioned Thr11, the phenyl ring of compound **6** occupies the position of histone residue Gly 12 (Fig. 6). Moreover, the protein loop Ala315-Ser320 relocates even more extensively than in the complex with compound **5**. Now, the phenyl ring of the ligand stacks in between two protein residues, His90 and Arg316, extending from the flexible loop. The histone binding site is divided into two subsites by the Arg316 side chain (Fig. 6). The ligand benzene ring points toward the solvent, and the Arg316 side chain occupies the histone's Ser10 position.

Such global change in the architecture of the binding site may compromise the enzyme's activity. The movement upon ligand binding may be associated with the enthalpic cost of binding energy characterized for this ligand. A ligand with a similar tail and carboxynicotinic acid core has been explored previously (PDB-Id 5FP7), but no such interactions with the enzyme's loop were observed [26]. There seems to be synergy between the ligand's core binding and the histone binding site.

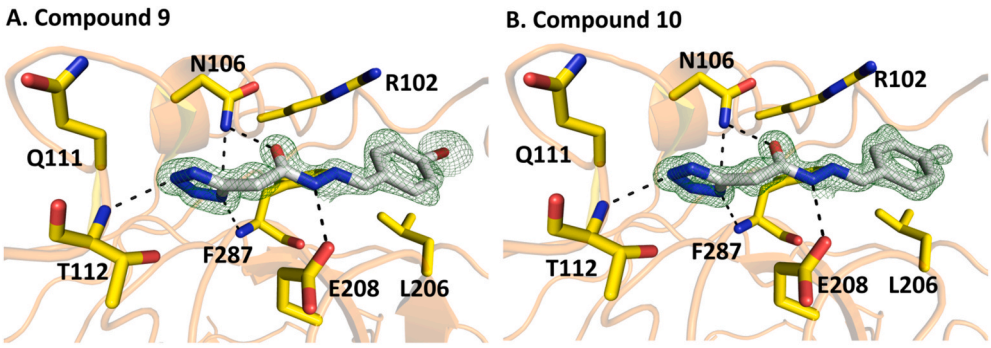

Fig. 5. Details of the interaction of compounds **9** and **10** in the distal binding pocket of KDM4D. Elements of the protein structure are depicted as semi-transparent orange ribbons, except for the side chains of the relevant amino acid residues, which are shown as yellow sticks. The presence of the ligand, also depicted as sticks, is evidenced by the 2mFo-DFc composite omit electron density map in green contoured at 1.2σ. Polar interactions between the ligand and the protein, water molecules, and metal ion are indicated as black dashed lines.

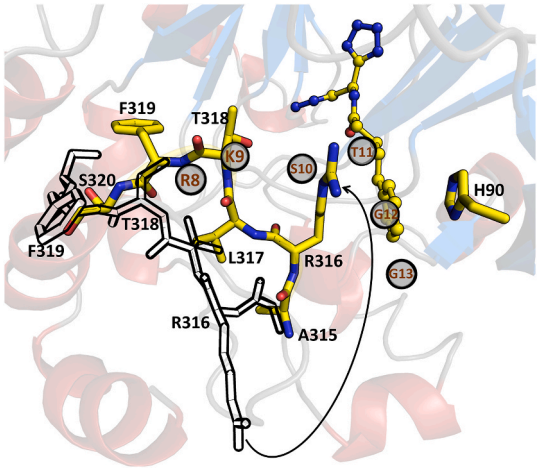

Fig. 6. Movement of the flexible loop Ala 315 – Ser 320 towards the histone binding site. The loop structures are taken from the complexes with compounds **6** and **4**. Elements of the protein structure are depicted as ribbons. The side chains of the loop and residue His90 taking part in stacking interactions in the structure with compound **6** are shown as yellow sticks. The superimposed loop from the structure with compound **4** is depicted in black and white. Superimposed elements from the structure PDB 4HON identify Cα positions of residues in a histone-derived peptide as grey spheres with red labels, showing that both compound **6** and the loop occupy positions of many residues of the bound histone peptide.

Also, a twofold interaction of the ligand with a Tyr136 residue achieved by placing the tetrazole ring into the 2OG binding site might be why the ligand's tail binds in such a defined way in the case of compound **6.** Despite the binding affinity of compound **6** of around 0.5 mM, the structural data provided us with precious information about the protein dynamics. The loop movement associated with ligand binding results in the formation of a stacking interaction between ligand and protein that was not observed before. This kind of structural information may prove helpful in designing molecules with increased selectivity towards KDM4D over other oxygenases. As there is a high degree of similarity within the conserved binding sites in multiple KDM enzymes, the major concern is developing selective inhibitors for particular enzymes. Thus, the selectivity determining part of the ligands should not be buried in the 2OG binding site but rather localized closer to the surface and the histone binding cavity. Interestingly, the His90 residue that forms the stacking interactions with our compound **6** occurs in KDM4D and KDM4E, while in KDM4A-C, it is substituted by an Asn residue. Another variable residue, Val 246, is positioned close to the ligand's benzene ring in KDM4D-E, while it is replaced by methionine in KDM4A-C. Moreover,

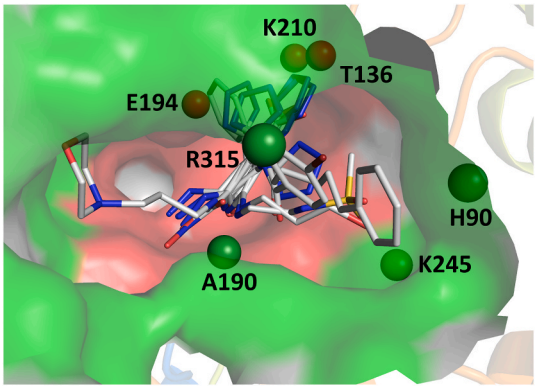

Fig. 7. Superimposition of all KDM4D-bound ligands. The histone binding site is depicted as surface, the catalytic site is colored red while the histone binding site is colored green. All ligands are superimposed and depicted as grey sticks. The positions of the ligand binding protein residues are shown as spheres, red for the core binding motifs and green for unique (except for Lys245) binding partners in the histone binding site.

the identified flexible loop could also serve as a selectivity marker for KDM4D as it differs from KDM4A-C.

Surprisingly, besides probing the histone binding site, KDM4D structures with compounds **9** and **10** indicated binding to a distal site localized on the protein surface opposite the active site. The importance of this cavity remains unknown, although its binding potential has been partially described before. A part of this cavity, occupied by the aromatic systems of both compounds **9** and **10**, has been mapped by the very low-occupancy modeled ligands as resulting of a fragment screening campaign (PDB codes: 5PHC, 5PHG, 5PHN) [49].

5. Conclusion

KDM4D, a representative of histone demethylase subfamily 4, has been chosen as a target enzyme for structural studies. The compounds investigated here are derivatives of high-affinity binding core motifs enriched with varying, outreaching tails. Interactions in the histone binding pocket were achieved by compound evolution, linking the core motifs with more flexible and chemically diverse moieties. This approach allowed us to overcome the binding barriers and locate unique interactions in the histone-binding site. These interactions may not be individually very strong but nevertheless may prove useful in designing molecular probes or lead compounds directed towards various oxygenases.

Crystallographic screening resulted in 10 hits, mostly bound close to the active site. Observed affinities covered a range from nanomolar

binding with a clearly defined electron density for the whole ligand to ligands only partially visible in the electron density because of the lack of a clearly preferred binding mode. Regions of KDM4D that may serve as targets for ligand selectivity enhancement were identified. It is known that crystallographic studies of chemically diverse ligands are essential for the inhibitor design process. As demonstrated here, the binding of some ligands may trigger the partial rearrangement of protein structural elements, such as loop movement, which would be very difficult to predict by docking algorithms. However, this structural plasticity of the target protein significantly impacts ligand binding and the inhibitor design process.

Moreover, using a carboxylic acid isostere as an alternative to already exploited motifs resulted in the discovery of a strong new binding motif. This may allow the evolution of existing molecules to obtain more desirable physiochemical and pharmacokinetic properties. As multiple oxygenases depend on the same co-substrate, 2OG, and many have a similar active-site architecture, the compounds from this screen may also prove useful for other enzymes.

6. Ancillary information

Supporting Information: (the list and the content of files supplied).
Supporting_Information
PDB ID Codes:
6F5R KDM4D-compound 1.
6F5Q KDM4D-compound 2.
6F5S KDM4D-compound 3.
6F5T KDM4D-compound 4.
6H11 KDM4D-compound 5.
6H0X KDM4D-compound 6.
6H0Y KDM4D-compound 7.
6H0W KDM4D-compound 8.
6H0Z KDM4D-compound 9.
6H10 KDM4D-compound 10.

7. Molecular formula strings

Molecular_Formula_Strings_Spreadsheet

Compound	SMILES	PDB ID
1	c1cnc(cc1C(=O)O)NCCCO	6F5R
2	CS(=O)(=O)NCCNc1cc(ccn1)C(=O)O	6F5Q
3	c1cnc(cc1c2n[nH]nn2)C(=O)NCCCN3CCOCC3	6F5S
4	c1cnc(cc1c2n[nH]nn2)C(=O)NO	6F5T
5	c1cc(ccc1C(=O)N[C@H](c2n[nH]nn2)C(=O)N[NH2])Br	6H11
6	c1ccc(*cc*1)CCCCC(=O)N[C@H](c2n[nH]nn2)C(=O)N[NH2]	6H0X
7	COc1ccc(*cc*1)C[C@H](c2n[nH]nn2)C(=O)NN	6H0Y
8	c1ccc(*cc*1)C[C@H](c2n[nH]nn2)C(=O)NN	6H0W
9	c1cc(ccc1/C=N/NC(=O)Cc2n[nH]nn2)Br	6H0Z
10	Cc1ccc(cc1)/C=N/NC(=O)Cc2n[nH]nn2	6H10

CRediT authorship contribution statement

Piotr H. Małecki: Writing – review & editing, Writing – original draft, Visualization, Validation, Supervision, Resources, Project administration, Methodology, Investigation, Funding acquisition, Formal analysis, Data curation, Conceptualization. **Georg M. Fassauer:** Writing – review & editing, Writing – original draft, Validation, Resources, Methodology, Investigation, Formal analysis. **Nicole Rüger:** Writing – review & editing, Resources, Methodology, Investigation, Formal analysis. **Lukas Schulig:** Writing – review & editing, Writing – original draft, Validation, Methodology, Investigation, Formal analysis, Data curation, Conceptualization. **Andreas Link:** Writing – review & editing, Writing – original draft, Validation, Supervision, Resources, Project administration, Methodology, Investigation, Funding acquisition, Formal analysis, Data curation, Conceptualization. **Oxana Krylova:** Writing – review & editing, Writing – original draft, Visualization, Validation, Methodology, Data curation. **Udo Heinemann:** Writing – review & editing, Writing – original draft, Supervision, Investigation, Funding acquisition, Formal analysis, Data curation. **Manfred S. Weiss:** Writing – review & editing, Writing – original draft, Visualization, Validation, Supervision, Resources, Project administration, Methodology, Investigation, Funding acquisition, Data curation, Conceptualization.

Declaration of competing interest

The authors declare that they have no known competing financial interests or personal relationships that could have appeared to influence the work reported in this paper.

Data availability

Data will be made available on request.

Acknowledgments

This work has been performed within the frame of the Joint Berlin MX Laboratory, a collaboration between several Berlin research institutions created to foster Structural Biology Research in the greater Berlin area. This research was co-funded by The National Science Centre Poland grant No: SONATA 2021/43/D/NZ7/02879 to P.H. Małecki. We thank Edgar Specker from the EU-OPENSCREEN Berlin facility for valuable discussion and advice. Our deep appreciation goes to Ulrich Gohlke and David Carter for expression constructs and KDM4D purification protocols prepared in the initial studies.

Appendix A. Supplementary data

Supplementary data to this article can be found online at https://doi.org/10.1016/j.ejmech.2024.116642.

References

[1] C. Dupont, D.R. Armant, C.A. Brenner, Epigenetics: definition, mechanisms and clinical perspective, Semin. Reprod. Med. 27 (2009) 351–357.
[2] C.H. Waddington, The genetic control of wing development in Drosophila, J. Genet. 41 (1940) 75–113.
[3] H. Sun, P.J. Kennedy, E.J. Nestler, Epigenetics of the depressed brain: role of histone acetylation and methylation, Neuropsychopharmacology 38 (2013) 124–137.
[4] B. Cheng, W. Pan, Y. Xiao, Z. Ding, Y. Zhou, X. Fei, J. Liu, Z. Su, X. Peng, J. Chen, HDAC-targeting epigenetic modulators for cancer immunotherapy, Eur. J. Med. Chem. 265 (2024) 116129.
[5] Y. Shi, J.R. Whetstine, Dynamic regulation of histone lysine methylation by demethylases, Mol. Cell. 25 (2007) 1–14.
[6] D.B. Seligson, S. Horvath, M.A. McBrian, V. Mah, H. Yu, S. Tze, Q. Wang, D. Chia, L. Goodglick, S.K. Kurdistani, Global levels of histone modifications predict prognosis in different cancers, Am. J. Pathol. 174 (2009) 1619–1628.
[7] G. Leszinski, U. Gezer, B. Siegele, O. Stoetzer, S. Holdenrieder, Relevance of histone marks H3K9me3 and H4K20me3 in cancer, Anticancer Res. 32 (2012) 2199–2205.
[8] H. Tamagawa, T. Oshima, M. Numata, N. Yamamoto, M. Shiozawa, S. Morinaga, Y. Nakamura, M. Yoshihara, Y. Sakuma, Y. Kameda, M. Akaike, N. Yukawa, Y. Rino, M. Masuda, Y. Miyagi, Global histone modification of H3K27 correlates with the outcomes in patients with metachronous liver metastasis of colorectal cancer, Eur. J. Surg. Oncol. 39 (2013) 655–661.
[9] W.L. Berry, R. Janknecht, KDM4/JMJD2 histone demethylases: epigenetic regulators in cancer cells, Cancer Res. 73 (2013) 2936–2942.
[10] Y. Tsukada, J. Fang, H. Erdjument-Bromage, M.E. Warren, C.H. Borchers, P. Tempst, Y. Zhang, Histone demethylation by a family of JmjC domain-containing proteins, Nature 439 (2006) 811–816.
[11] L. Hillringhaus, W.W. Yue, N.R. Rose, S.S. Ng, C. Gileadi, C. Loenarz, S.H. Bello, J. E. Bray, C.J. Schofield, U. Oppermann, Structural and evolutionary basis for the dual substrate selectivity of human KDM4 histone demethylase family, J. Biol. Chem. 286 (2011) 41616–41625.
[12] J.R. Whetstine, A. Nottke, F. Lan, M. Huarte, S. Smolikov, Z. Chen, E. Spooner, E. Li, G. Zhang, M. Colaiacovo, Y. Shi, Reversal of histone lysine trimethylation by the JMJD2 family of histone demethylases, Cell 125 (2006) 467–481.
[13] R.M. Labbe, A. Holowatyj, Z.Q. Yang, Histone lysine demethylase (KDM) subfamily 4: structures, functions and therapeutic potential, Am J Transl Res 6 (2013) 1–15.

[14] N. Iwamori, M. Zhao, M.L. Meistrich, M.M. Matzuk, The testis-enriched histone demethylase, KDM4D, regulates methylation of histone H3 lysine 9 during spermatogenesis in the mouse but is dispensable for fertility, Biol. Reprod. 84 (2011) 1225–1234.
[15] S. Shin, R. Janknecht, Diversity within the JMJD2 histone demethylase family, Biochem. Biophys. Res. Commun. 353 (2007) 973–977.
[16] J. Yang, A.M. Jubb, L. Pike, F.M. Buffa, H. Turley, D. Baban, R. Leek, K.C. Gatter, J. Ragoussis, A.L. Harris, The histone demethylase JMJD2B is regulated by estrogen receptor alpha and hypoxia, and is a key mediator of estrogen induced growth, Cancer Res. 70 (2010) 6456–6466.
[17] J.C. Black, A.L. Manning, C. Van Rechem, J. Kim, B. Ladd, J. Cho, C.M. Pineda, N. Murphy, D.L. Daniels, C. Montagna, P.W. Lewis, K. Glass, C.D. Allis, N.J. Dyson, G. Getz, J.R. Whetstine, KDM4A lysine demethylase induces site-specific copy gain and rereplication of regions amplified in tumors, Cell 154 (2013) 541–555.
[18] D.M. Carter, E. Specker, P.H. Malecki, J. Przygodda, K. Dudaniec, M.S. Weiss, U. Heinemann, M. Nazare, U. Gohlke, Enhanced properties of a benzimidazole benzylpyrazole lysine demethylase inhibitor: mechanism-of-action, binding site analysis, and activity in cellular models of prostate cancer, J. Med. Chem. 64 (2021) 14266–14282.
[19] A. Kawamura, M. Munzel, T. Kojima, C. Yapp, B. Bhushan, Y. Goto, A. Tumber, T. Katoh, O.N. King, T. Passioura, L.J. Walport, S.B. Hatch, S. Madden, S. Muller, P. E. Brennan, R. Chowdhury, R.J. Hopkinson, H. Suga, C.J. Schofield, Highly selective inhibition of histone demethylases by de novo macrocyclic peptides, Nat. Commun. 8 (2017) 14773.
[20] A.T. Hauser, D. Robaa, M. Jung, Epigenetic small molecule modulators of histone and DNA methylation, Curr. Opin. Chem. Biol. 45 (2018) 73–85.
[21] H.U. Kaniskan, M.L. Martini, J. Jin, Inhibitors of protein methyltransferases and demethylases, Chem. Rev. 118 (2018) 989–1068.
[22] H. Lin, Q. Li, Q. Li, J. Zhu, K. Gu, X. Jiang, Q. Hu, F. Feng, W. Qu, Y. Chen, H. Sun, Small molecule KDM4s inhibitors as anti-cancer agents, J. Enzym. Inhib. Med. Chem. 33 (2018) 777–793.
[23] P.A. Cloos, J. Christensen, K. Agger, A. Maiolica, J. Rappsilber, T. Antal, K. H. Hansen, K. Helin, The putative oncogene GASC1 demethylates tri- and dimethylated lysine 9 on histone H3, Nature 442 (2006) 307–311.
[24] N.R. Rose, S.S. Ng, J. Mecinovic, B.M. Lienard, S.H. Bello, Z. Sun, M. A. McDonough, U. Oppermann, C.J. Schofield, Inhibitor scaffolds for 2-oxoglutarate-dependent histone lysine demethylases, J. Med. Chem. 51 (2008) 7053–7056.
[25] C. Jin, L. Yang, M. Xie, C. Lin, D. Merkurjev, J.C. Yang, B. Tanasa, S. Oh, J. Zhang, K.A. Ohgi, H. Zhou, W. Li, C.P. Evans, S. Ding, M.G. Rosenfeld, Chem-seq permits identification of genomic targets of drugs against androgen receptor regulation selected by functional phenotypic screens, Proc. Natl. Acad. Sci. U.S.A. 111 (2014) 9235–9240.
[26] S.M. Westaway, A.G. Preston, M.D. Barker, F. Brown, J.A. Brown, M. Campbell, C. W. Chung, H. Diallo, C. Douault, G. Drewes, R. Eagle, L. Gordon, C. Haslam, T. G. Hayhow, P.G. Humphreys, G. Joberty, R. Katso, L. Kruidenier, M. Leveridge, J. Liddle, J. Mosley, M. Muelbaier, R. Randle, I. Rioja, A. Rueger, G.A. Seal, R. J. Sheppard, O. Singh, J. Taylor, P. Thomas, D. Thomson, D.M. Wilson, K. Lee, R. K. Prinjha, Cell penetrant inhibitors of the KDM4 and KDM5 families of histone lysine demethylases. 1. 3-Amino-4-pyridine carboxylate derivatives, J. Med. Chem. 59 (2016) 1357–1369.
[27] P.H. Malecki, N. Rüger, M. Roatsch, O. Krylova, A. Link, M. Jung, U. Heinemann, M.S. Weiss, Structure-based screening of tetrazolylhydrazide inhibitors versus KDM4 histone demethylases, ChemMedChem 14 (2019) 1828–1839.
[28] N. Rüger, M. Roatsch, T. Emmrich, H. Franz, R. Schule, M. Jung, A. Link, Tetrazolylhydrazides as selective fragment-like inhibitors of the JumonjiC-domain-containing histone demethylase KDM4A, ChemMedChem 10 (2015) 1875–1883.
[29] C.W. Murray, D.C. Rees, The rise of fragment-based drug discovery, Nat. Chem. 1 (2009) 187–192.
[30] L. Kollar, M. Gobec, B. Szilagyi, M. Proj, D. Knez, P. Abranyi-Balogh, L. Petri, T. Imre, D. Bajusz, G.G. Ferenczy, S. Gobec, G.M. Keseru, I. Sosic, Discovery of selective fragment-sized immunoproteasome inhibitors, Eur. J. Med. Chem. 219 (2021) 113455.
[31] N. Rüger, G.M. Fassauer, C. Bock, T. Emmrich, A. Bodtke, A. Link, Substituted tetrazoles as multipurpose screening compounds, Mol. Divers. 21 (2017) 9–27.
[32] J. Büchi, P. Labhart, L. Ragaz, Zur kenntnis lokalanästhetisch wirksamer pyridin-4-carbonsäure-derivate, Helv. Chim. Acta 30 (1947) 507–519.
[33] G. Heinisch, G. Lötsch, Entscheidende Steigerung der Regioselektivität bei radikalischen Substitutionen: Minisci-Reaktion im Zweiphasensystem, Angew. Chem. 97 (1985) 694–695.
[34] A.N. Terpigorev, I.V. Tselinskii, A.V. Makarevich, G.M. Frolova, A.A. Melnikov, Tetraazolylnitromethanes .1. Synthesis of 5-tetraazolylnitromethanes and their methylation with diazomethane, Zh. Org. Khim. 23 (1987) 244–254.
[35] A.C. Biraboneye, S. Madonna, Y. Laras, S. Krantic, P. Maher, J.-L. Kraus, Potential neuroprotective drugs in cerebral ischemia: new saturated and polyunsaturated lipids coupled to hydrophilic moieties: synthesis and biological activity, J. Med. Chem. 52 (2009) 4358–4369.
[36] T.Y. Teng, Mounting of crystals for macromolecular crystallography in a free-standing thin film, J. Appl. Crystallogr. 23 (1990) 387–391.
[37] U. Mueller, R. Förster, M. Hellmig, F.U. Huschmann, A. Kastner, P. Malecki, S. Pühringer, M. Röwer, K. Sparta, M. Steffien, M. Ühlein, P. Wilk, M.S. Weiss, The macromolecular crystallography beamlines at BESSY II of the Helmholtz-Zentrum Berlin: Current status and perspectives, Eur Phys J Plus (2015) 130–`141.
[38] K.M. Sparta, M. Krug, U. Heinemann, U. Mueller, M.S. Weiss, XDSAPP2.0, J. Appl. Crystallogr. 49 (2016) 1085–1092.
[39] A.J. McCoy, R.W. Grosse-Kunstleve, P.D. Adams, M.D. Winn, L.C. Storoni, R. J. Read, Phaser crystallographic software, J. Appl. Crystallogr. 40 (2007) 658–674.
[40] G.N. Murshudov, P. Skubak, A.A. Lebedev, N.S. Pannu, R.A. Steiner, R.A. Nicholls, M.D. Winn, F. Long, A.A. Vagin, REFMAC5 for the refinement of macromolecular crystal structures, Acta Crystallogr D Biol Crystallogr 67 (2011) 355–367.
[41] M.D. Winn, C.C. Ballard, K.D. Cowtan, E.J. Dodson, P. Emsley, P.R. Evans, R. M. Keegan, E.B. Krissinel, A.G. Leslie, A. McCoy, S.J. McNicholas, G.N. Murshudov, N.S. Pannu, E.A. Potterton, H.R. Powell, R.J. Read, A. Vagin, K.S. Wilson, Overview of the CCP4 suite and current developments, Acta Crystallogr D Biol Crystallogr 67 (2011) 235–242.
[42] P. Emsley, B. Lohkamp, W.G. Scott, K. Cowtan, Features and development of coot, Acta Crystallogr D Biol Crystallogr 66 (2010) 486–501.
[43] P.V. Afonine, R.W. Grosse-Kunstleve, N. Echols, J.J. Headd, N.W. Moriarty, M. Mustyakimov, T.C. Terwilliger, A. Urzhumtsev, P.H. Zwart, P.D. Adams, Towards automated crystallographic structure refinement with phenix.refine, Acta Crystallogr D Biol Crystallogr 68 (2012) 352–367.
[44] J.W.C.-M. Benbow, Y. Margaret, Kung, W. Daniel, Substituted 4-amino[1,2,4]triazolo[4,3-a] quinoxalines, in: U.S. Patent No. 20040192698, 2004.
[45] S. Krishnan, R.C. Trievel, Structural and functional analysis of JMJD2D reveals molecular basis for site-specific demethylation among JMJD2 demethylases, Structure 21 (2013) 98–108.
[46] V. Bavetsias, R.M. Lanigan, G.F. Ruda, B. Atrash, M.G. McLaughlin, A. Tumber, N. Y. Mok, Y.V. Le Bihan, S. Dempster, K.J. Boxall, F. Jeganathan, S.B. Hatch, P. Savitsky, S. Velupillai, T. Krojer, K.S. England, J. Sejberg, C. Thai, A. Donovan, A. Pal, G. Scozzafava, J.M. Bennett, A. Kawamura, C. Johansson, A. Szykowska, C. Gileadi, N.A. Burgess-Brown, F. von Delft, U. Oppermann, Z. Walters, J. Shipley, F.I. Raynaud, S.M. Westaway, R.K. Prinjha, O. Fedorov, R. Burke, C.J. Schofield, I. M. Westwood, C. Bountra, S. Muller, R.L. van Montfort, P.E. Brennan, J. Blagg, 8-Substituted pyrido[3,4-d]pyrimidin-4(3H)-one derivatives as potent, cell permeable, KDM4 (JMJD2) and KDM5 (JARID1) histone lysine demethylase inhibitors, J. Med. Chem. 59 (2016) 1388–1409.
[47] M. Nishio, Y. Umezawa, J. Fantini, M.S. Weiss, P. Chakrabarti, CH–π hydrogen bonds in biological macromolecules, Phys. Chem. Chem. Phys. 16 (2014) 12648–12683.
[48] S. Shen, A.P. Kozikowski, Why hydroxamates may not Be the best histone deacetylase inhibitors–what some may have forgotten or would rather forget? ChemMedChem 11 (2016) 15–21.
[49] N.M. Pearce, T. Krojer, A.R. Bradley, P. Collins, R.P. Nowak, R. Talon, B. D. Marsden, S. Kelm, J. Shi, C.M. Deane, F. von Delft, A multi-crystal method for extracting obscured crystallographic states from conventionally uninterpretable electron density, Nat. Commun. 8 (2017) 15123.